Draft version November 8, 2018
Typeset using LaTeX **twocolumn** style in AASTeX61

OCCURRENCE OF RADIO MINIHALOS IN A MASS-LIMITED SAMPLE OF GALAXY CLUSTERS

Simona Giacintucci,[1] Maxim Markevitch,[2] Rossella Cassano,[3] Tiziana Venturi,[3] Tracy E. Clarke,[1] and Gianfranco Brunetti[3]

[1] *Naval Research Laboratory, 4555 Overlook Avenue SW, Code 7213, Washington, DC 20375, USA*
[2] *NASA/Goddard Space Flight Center, Greenbelt, MD 20771, USA*
[3] *INAF - Istituto di Radioastronomia, via Gobetti 101, I-40129 Bologna, Italy*

(Received December 20, 2016; Revised April 6, 2017; Accepted November 8, 2018)

Submitted to ApJ

ABSTRACT

We investigate the occurrence of radio minihalos — diffuse radio sources of unknown origin observed in the cores of some galaxy clusters — in a statistical sample of 58 clusters drawn from the *Planck* Sunyaev-Zel'dovich cluster catalog using a mass cut ($M_{500} > 6 \times 10^{14} M_{\odot}$). We supplement our statistical sample with a similarly-sized non-statistical sample mostly consisting of clusters in the ACCEPT X-ray catalog with suitable X-ray and radio data, which includes lower-mass clusters. Where necessary (for 9 clusters), we reanalyzed the *Very Large Array* archival radio data to determine if a mihinalo is present. Our total sample includes all 28 currently known and recently discovered radio minihalos, including 6 candidates. We classify clusters as cool-core or non-cool core according to the value of the specific entropy floor in the cluster center, rederived or newly derived from the *Chandra* X-ray density and temperature profiles where necessary (for 27 clusters). Contrary to the common wisdom that minihalos are rare, we find that almost all cool cores — at least 12 out of 15 (80%) — in our complete sample of massive clusters exhibit minihalos. The supplementary sample shows that the occurrence of minihalos may be lower in lower-mass cool-core clusters. No minihalos are found in non-cool-cores or "warm cores". These findings will help test theories of the origin of minihalos and provide information on the physical processes and energetics of the cluster cores.

Keywords: catalogs — galaxies: clusters: general — surveys — X-rays: galaxies: clusters — radio continuum: galaxies: clusters

Corresponding author: Simona Giacintucci
simona.giacintucci@nrl.navy.mil

1. INTRODUCTION

A striking feature of a number of galaxy clusters is the presence of diffuse synchrotron radiation in the form of large peripheral radio relics and two classes of centrally-located radio sources — Mpc-size *giant radio halos* and smaller-scale *minihalos* (see Feretti et al. 2012, for a review). The importance of these extended, steep spectrum[1] radio sources is nowadays widely recognized as their existence requires magnetic fields and ultra-relativistic electrons to be distributed throughout a large fraction of the cluster volume (e.g., Brunetti & Jones 2014).

Giant radio halos are associated with unrelaxed clusters (e.g., Cassano et al. 2010, 2013; Kale et al. 2015; Parekh et al. 2015; Cuciti et al. 2015; Yuan et al. 2015) without a central cool core (Rossetti et al. 2013), with a few possible outliers (Bonafede et al. 2014; Kale & Parekh 2016, Sommer et al. 2017). Minihalos, instead, are typically found in globally relaxed, cool-core clusters (e.g., Gitti et al. 2002; Govoni et al. 2009; Hlavacek-Larrondo et al. 2013; Giacintucci et al. 2014a; van Weeren et al. 2014; Kale et al. 2015; Yuan et al. 2015). Their emission envelops the central active radio galaxy, nearly always found at the center of a cool-core cluster (e.g., Mittal et al. 2009), and extends quite far from it (r ∼50–300 kpc), typically filling the cluster cooling region. Minihalos are faint and usually quite amorphous in shape, thus very different from typical extended radio galaxies with lobes and jets. Minihalos also differ from the *dying* radio galaxies that are sometimes found at the cluster centers, whose extended emission typically has an ultra-steep radio spectrum ($\alpha_{\rm radio} \gtrsim 2$) and a morphology that somehow preserves the original lobed structure of the active phase, when the source was still fed by the central nucleus (e.g., Saikia & Jamrozy 2009, Murgia et al. 2011, 2012).

Minihalos often appear bounded by one or two X-ray cold fronts (Mazzotta & Giacintucci 2008; Giacintucci et al. 2014a,b) that result from sloshing of the cool gas in the central core (e.g., Ascasibar & Markevitch 2006). Based on this coincidence, it has been proposed that minihalos arise from the reacceleration of seed relativistic electrons in the magnetized cool core (Gitti et al. 2002, 2004) by sloshing-induced turbulence (Mazzotta & Giacintucci 2008; ZuHone et al. 2013; Giacintucci et al. 2014b). Numerical simulations show that sloshing motions can amplify magnetic fields and develop turbulence in the area enclosed by the cold fronts, which may lead to the generation of diffuse radio emission confined to the sloshing region (ZuHone et al. 2013). A recent direct measurement of the gas velocities in the Perseus cool core with the *Hitomi* X-ray satellite revealed the presence of turbulence sufficient for the above scenario, and possibly for balancing the radiative cooling in the core (Hitomi Collaboration et al. 2016). An alternative explanation of minihalos is hadronic models (e.g., Pfrommer & Ensslin 2004; Fujita et al. 2007; Zandanel et al. 2014), where the radio-emitting electrons are generated through the interaction of cosmic ray (CR) protons with the thermal protons in the intracluster medium. Both turbulence and CR protons should also contribute to balancing the radiative cooling in the cluster cores (e.g., Zhuravleva et al. 2014; Fujita & Ohira 2011; Guo & Oh 2008; Jacob & Pfrommer 2017a). Thus the relation between radio minihalos and cool cores may exist at a fundamental level (e.g., Bravi et al. 2016, Fujita & Ohira 2013), making these radio phenomena important for understanding the physics of cool cores.

The study of minihalos has been limited by their small number (e.g., Gitti et al. 2004; Cassano et al. 2008; Govoni et al. 2009), with only about 10 confirmed detections as of 2011 (Feretti et al. 2012). The number of known minihalos has then rapidly increased, with 22 confirmed detections[2] and 6 candidates up to date (Hlavacek-Larrondo et al. 2013; Giacintucci et al. 2014a; van Weeren et al. 2014; Kale et al. 2015, Pandey-Pommier et al. 2016), including two new minihalos and one candidate detection that will be presented in a forthcoming paper (Giacintucci et al. 2017, hereafter G17).

The new detections have allowed exploratory investigations of the statistical properties of minihalos and of their host clusters (Giacintucci et al. 2014a; Yuan et al. 2015; Kale et al. 2015; Gitti et al. 2015; Bravi et al. 2016; Jacob & Pfrommer 2017a,b), that support the association of minihalos with relaxed, cool-core clusters. Furthermore, it has been noted that minihalos tend to be observed in the most massive and hottest clusters with cool cores (Giacintucci et al. 2014a). If true, this observation will provide a constraint to discriminate between different models for the minihalo origin. In a broader context, it can provide information on the energy budget and physical processes in

[1] $\alpha_{\rm radio} > 1$, for $S_\nu \propto \nu^{-\alpha_{\rm radio}}$, where S_ν is the flux density at the frequency ν and $\alpha_{\rm radio}$ is the radio spectral index.

[2] The former minihalo in A 2390 (Bacchi et al. 2003) is excluded because it was recently found to be larger (Sommer et al. 2017), borderline between giant halos (as defined in Cassano & Brunetti 2005) and minihalos. We note that this cluster has an unusually large cool core (Vikhlinin et al. 2005), comparable in size to the diffuse radio source.

the cluster cool cores, where the radiative cooling is believed to be balanced by some non-gravitational heating source(s) (e.g., McNamara & Nulsen 2007). The aim of the present work is to quantify this observation in a statistical way. For this purpose, we have selected a complete, mass-limited sample of 75 clusters from the *Planck* Sunyaev-Zel'dovich (SZ) cluster catalog (Planck Collaboration et al. 2014) and performed an X-ray and radio analysis of the majority of the sample members (77%) that have *Chandra* data. We complemented this *Chandra* statistical sample with a large additional sample of 48 clusters in the ACCEPT[3] X-ray catalog (Cavagnolo et al. 2009, hereafter C09), with suitable radio data, plus the Phoenix cluster (SPT-CL J2344-4243, McDonald et al. 2015), for a total of 106 clusters. Where necessary (for 27 clusters), we used the X-ray *Chandra* data to derive the profiles of gas density, temperature and specific entropy. For those clusters in both samples without published radio observations on the minihalo angular scales, we used archival *Very Large Array* (*VLA*) data to investigate the presence of a minihalo and present the results here (no minihalos were detected). We also include in our analysis the 3 new minihalo detections with the *Giant Metrewave Radio Telescope* that that will be presented in G17. We then compared the cluster mass and X-ray properties with the presence of a minihalo for our mass-limited as well as combined samples.

We adopt a ΛCDM cosmology with H_0=70 km s^{-1} Mpc^{-1}, $\Omega_m = 0.3$ and $\Omega_\Lambda = 0.7$. All errors are quoted at the 68% confidence level.

2. DEFINITION OF A MINIHALO

To distinguish minihalos from other diffuse radio phenomena in clusters, such as radio galaxies (in active or dying phase), large radio halos, and relics, we use the following physically-motivated definition. A minihalo is a diffuse radio source at the cluster center with the following properties:

1. The emission does not consist of radio lobes or tails, nor does it show, at any angular resolution, any morphological connection (jets) to the central AGN (such sources would be radio galaxies).

2. The minimum radius of approximately 50 kpc. At smaller radii, diffusion and other transport mechanisms, such as sloshing motions, can plausibly spread the relativistic electrons from the central AGN within their synchrotron radiative cooling time (e.g., see §6.4 in Giacintucci et al. 2014a) without the need for additional physics.

3. The maximum radius of $0.2R_{500}$.[4] This radius separates two physically distinct cluster regions. Based on X-ray and SZ observations, density, temperature and pressure profiles of the thermal intracluster medium (ICM) outside this radius are self-similar, whereas a large scatter of the ICM profiles is observed at $r \lesssim 0.2R_{500}$ (e.g., McDonald et al. 2017 and references therein). This is caused by the increased importance of non-gravitational processes such as cooling, AGN and stellar feedback in the cores. Thus, diffuse radio emission that is confined within this radius can have a different origin, possibly related to processes in the core, from the emission on a larger scale (halos and peripheral relics). The bulk of the emission of large radio halos originates well outside $r = 0.2R_{500}$ (e.g., Cassano et al. 2007).

To determine whether a diffuse source fits the above definition we need radio data of a certain minimum quality. For item 1, we need sufficiently high resolution to image the range of scales from few tens of kpc to few kpc in order to determine the morphology of the central radio galaxy and rule out the possibility of the diffuse emission being part of it. It is also needed to discriminate between genuine diffuse emission and a blend of individual radio galaxies in (or projected onto) the core and remove their contribution as well as that of the central radio galaxy. At the same time, for items 2 and 3, sensitive, lower-resolution radio observations with a good sampling of the *uv* plane, particularly at short antenna spacings (that correspond to larger angular scales in the sky), are crucial to detect diffuse emission on a larger scale, including the scales beyond our adopted maximum size for the minihalo.

The size of the radio source that we use here is estimated as $R_{\rm radio} = \sqrt{R_{\rm max} R_{\rm min}}$, where $R_{\rm max}$ and $R_{\rm min}$ are the maximum and minimum radii of the 3σ surface brightness isocontour (Cassano et al. 2007). It obviously depends on the *uv* coverage of the data and the noise level of the image. As detailed in §3, a large fraction of the clusters in our statistical sample have already been reported to have either a large radio halo (well above $0.2R_{500}$) or a non-detection based on high-sensitivity low- and high-resolution images, which is sufficient for our classification purpose. For the remaining clusters

[3] Archive of Chandra Cluster Entropy Profile Tables.

[4] R_{500} is the radius that encloses a mean overdensity of 500 with respect to the critical density at the cluster redshift.

(except Perseus and Phoenix), which include all minihalos and ambiguous classifications from the literature, as well as clusters with no published radio images at the needed resolution, we have uniformly analyzed new and archival radio data, with results presented in this paper (§6), Giacintucci et al. (2014a) and G17. The halo sizes come from those analyses. As shown in Appendices A and B, the data used for this paper, while heterogeneous, have sufficient sensitivity and a range of angular resolutions, as well as good sampling of short baselines in the *uv* plane, and thus would allow us to detect diffuse emission at the typical brightness on the core scale and, in most cases, at the larger scale of the giant halos. Furthermore, our measured minihalo sizes do not correlate with the signal-to-noise ratio of the radio images (Appendix B). This gives us assurance that the radio extent is not determined by the image sensitivity — the minihalos are intrinsically smaller than halos (see also Murgia et al. 2009). Of course, we cannot rule out the possibility that deeper data would uncover large-scale emission much fainter than the current radio halos in some of the sources that we classify here as minihalos. However, in a few very well-observed minihalos, we do see evidence for an abrupt drop of the radio brightness at a certain radius (Giacintucci et al. 2011, 2014b), which suggests that the minihalo extent has a physical significance.

3. CLUSTER SELECTION

To quantify the earlier observation that mihihalos are preferentially found in massive cool core systems (Giacintucci et al. 2014a), in this paper we use a combination of two samples. One is a statistically complete, mass-limited sample of massive clusters, while the other is a similarly-sized arbitrary sample of clusters that do not satisfy some of the criteria for the complete sample, but do have high-quality radio and X-ray data and thus can increase the confidence of any correlations that we may find. The latter sample extends to lower masses, which is obviously helpful for investigating any correlation of the minihalo occurrence with the cluster mass. As we will see, the *completeness* of the sample at lower masses is not critical for the conclusions of this work, while the completeness of the high-mass sample, used for the statistical analysis, is.

Table 1. Statistical Sample

Planck name PSZ1	Alternative name	RA_{J2000} (h,m,s)	DEC_{J2000} (deg, ′,″)	z	M_{500} (10^{14} $M_\odot$)	R_{500} (Mpc)	Central diffuse radio emission	R_{radio}/R_{500}	Radio reference
Clusters with *Chandra* observations									
G009.02−81.22	A 2744	00 14 13.3	−30 22 31	0.307	$9.6^{+0.5}_{-0.5}$	1.35	halo	0.6	3, 4
G116.90−53.55	A 68	00 36 57.7	+09 08 37	0.255	$6.2^{+0.6}_{-0.7}$	1.19	no detection	···	5
G106.84−83.24	A 2813	00 43 27.4	−20 37 27	0.292	$9.2^{+0.5}_{-0.5}$	1.34	no detection	···	6
G212.97−84.04	A 2895	01 18 10.8	−26 58 28	0.228	$6.1^{+0.5}_{-0.5}$	1.19	no detection	···	6
G159.81−73.47	A 209	01 31 53.4	−13 34 27	0.206	$8.2^{+0.4}_{-0.4}$	1.33	halo	0.4	7, 8
G138.35−39.80	RXC J0142.0+2131	01 42 11.6	+21 32 32	0.280	$6.1^{+0.8}_{-0.8}$	1.17	no detection	···	9
G210.08−60.96	MACS J0257.6−2209	02 57 40.3	−22 09 46	0.322	$7.2^{+0.7}_{-0.7}$	1.22	halo (c)	···	10, 11
G164.20−38.90	A 401	02 58 54.8	+13 32 24	0.074	$6.8^{+0.3}_{-0.3}$	1.31	halo	0.3	2, 12
G223.91−60.09	A 3088	03 07 03.2	−28 40 24	0.254	$6.7^{+0.6}_{-0.6}$	1.22	no detection	···	8
G171.96−40.64	···	03 13 00.3	+08 22 53	0.270	$11.1^{+0.6}_{-0.6}$	1.44	halo	0.4	13
G182.42−28.28	A 478	04 13 25.2	+10 28 19	0.088	$7.1^{+0.3}_{-0.4}$	1.32	minihalo	0.1	14
G208.80−30.67	A 521	04 54 05.0	−10 13 35	0.248	$6.9^{+0.6}_{-0.6}$	1.24	halo	0.6	15, 16
G195.78−24.29	A 520	04 54 15.9	+02 57 10	0.203	$7.1^{+0.6}_{-0.6}$	1.27	halo	0.4	17
G208.59−26.00	RXC J0510.7−0801	05 10 44.3	−08 01 12	0.220	$7.4^{+0.6}_{-0.6}$	1.28	bad data	···	5
G215.29−26.09	RXC J0520.7−1328	05 20 47.2	−13 30 08	0.336	$6.1^{+0.8}_{-0.8}$	1.15	bad data	···	18
G139.61+24.20	···	06 22 13.9	+74 41 39	0.267	$7.1^{+0.6}_{-0.6}$	1.24	minihalo (c)	0.04	2
G149.75+34.68	A 665	08 30 50.9	+65 52 01	0.182	$8.2^{+0.4}_{-0.4}$	1.34	halo	0.5	19
G186.37+37.26	A 697	08 42 59.6	+36 21 10	0.282	$11.5^{+0.5}_{-0.5}$	1.45	halo	0.4	20, 6, 7
G239.29+24.75	A 754	09 08 56.2	−09 40 21	0.054	$6.7^{+0.2}_{-0.2}$	1.31	halo	0.5	21, 12, 22
G166.11+43.40	A 773	09 18 04.5	+51 42 15	0.217	$7.1^{+0.4}_{-0.5}$	1.26	halo	0.4	3
G195.60+44.03	A 781	09 20 16.0	+30 29 56	0.295	$6.4^{+0.6}_{-0.6}$	1.18	halo (c)	0.4	23, 24

Table 1 continued

Table 1 *(continued)*

Planck name PSZ1	Alternative name	RA_{J2000} (h,m,s)	DEC_{J2000} (deg, ′,″)	z	M_{500} (10^{14} $M_\odot$)	R_{500} (Mpc)	Central diffuse radio emission	R_{radio}/R_{500}	Radio reference
G135.03+36.03	RBS 797	09 47 00.2	+76 23 44	0.345	$6.3^{+0.6}_{-0.7}$	1.16	minihalo	0.1	2, 25, 26
G266.85+25.06	A 3444	10 23 54.8	−27 17 09	0.254	$7.6^{+0.5}_{-0.6}$	1.27	minihalo	0.1	2, 1, 5, 6
G149.21+54.17	A 1132	10 58 25.9	+56 48 09	0.137	$6.2^{+0.3}_{-0.3}$	1.24	no detection	···	19
G257.13+55.63	RXC J1115.8+0129	11 15 54.9	+01 29 56	0.350	$6.4^{+0.7}_{-0.7}$	1.16	minihalo (c)	···	27
G278.58+39.15	A 1300	11 31 55.8	−19 55 42	0.308	$8.8^{+0.6}_{-0.6}$	1.31	halo	0.4	4, 28, 29
G139.17+56.37	A 1351	11 42 24.5	+58 31 41	0.322	$7.1^{+0.5}_{-0.5}$	1.21	halo	0.4	30, 7
G180.56+76.66	A 1423	11 57 19.9	+33 36 39	0.214	$6.1^{+0.5}_{-0.5}$	1.20	no detection	···	6
G229.70+77.97	A 1443	12 01 21.1	+23 06 31	0.269	$7.7^{+0.5}_{-0.6}$	1.27	halo	0.5	31
G289.19+72.19	RXC J1234.2+0947	12 34 31.8	+09 46 23	0.229	$6.0^{+0.6}_{-0.6}$	1.19	halo (c)	0.3	5
G114.99+70.36	A 1682	13 06 54.9	+46 31 33	0.226	$6.2^{+0.4}_{-0.5}$	1.20	halo (c)	0.4	32, 4, 33
G313.33+61.13	A 1689	13 11 26.5	−01 20 11	0.183	$8.9^{+0.4}_{-0.4}$	1.38	halo	0.5	2, 34
G323.30+63.65	A 1733	13 27 00.7	+02 12 14	0.259	$7.1^{+0.6}_{-0.7}$	1.24	no data	···	···
G107.14+65.29	A 1758a	13 32 39.5	+50 32 47	0.280	$8.0^{+0.4}_{-0.5}$	1.28	halo	0.6	4,7
G092.67+73.44	A 1763	13 35 18.1	+41 00 10	0.228	$8.3^{+0.4}_{-0.4}$	1.32	no detection	···	6
G340.37+60.57	A 1835	14 01 02.7	+02 51 56	0.253	$8.5^{+0.5}_{-0.6}$	1.32	minihalo	0.18	2, 35
G067.19+67.44	A 1914	14 26 03.9	+37 49 35	0.171	$7.0^{+0.4}_{-0.4}$	1.28	halo	0.5	12
G340.94+35.10	AS 780	14 59 30.4	−18 08 58	0.236	$7.7^{+0.6}_{-0.6}$	1.29	minihalo	0.04	5, 2, 8
G355.07+46.20	RXC J1504.1−0248	15 04 05.4	−02 47 54	0.215	$7.0^{+0.6}_{-0.6}$	1.26	minihalo	0.11	36
G006.45+50.56	A 2029	15 10 50.8	+05 44 43	0.077	$6.8^{+0.2}_{-0.2}$	1.30	minihalo	0.19	2, 35
G346.61+35.06	RXC J1514.9−1523	15 15 00.4	−15 21 29	0.223	$8.3^{+0.5}_{-0.6}$	1.33	halo	0.5	37
G044.24+48.66	A 2142	15 58 25.6	+27 14 25	0.089	$8.8^{+0.3}_{-0.3}$	1.42	halo	0.3	38, 39
G006.76+30.45	A 2163	16 15 49.2	−06 09 09	0.203	$16.4^{+0.4}_{-0.4}$	1.68	halo	0.7	40
G021.10+33.24	A 2204	16 32 47.8	+05 35 32	0.151	$8.0^{+0.4}_{-0.4}$	1.34	minihalo	0.04	14
G097.72+38.13	A 2218	16 35 52.0	+66 11 44	0.171	$6.4^{+0.3}_{-0.3}$	1.24	halo	0.3	2, 19
G072.61+41.47	A 2219	16 40 18.6	+46 41 55	0.228	$11.0^{+0.4}_{-0.4}$	1.45	halo	0.6	12
G110.99+31.74	A 2256	17 04 08.1	+78 38 07	0.058	$6.3^{+0.2}_{-0.2}$	1.28	halo	0.4	41, 42
G049.22+30.84	RXC J1720.1+2637	17 20 12.6	+26 37 23	0.164	$6.3^{+0.4}_{-0.4}$	1.24	minihalo	0.1	43
G055.58+31.87	A 2261	17 22 21.9	+32 07 58	0.224	$7.4^{+0.4}_{-0.5}$	1.28	halo	0.4	44
G094.00+27.41	CL 1821+643	18 22 00.4	+64 20 34	0.332	$6.3^{+0.4}_{-0.4}$	1.16	halo	0.4	45, 46
G018.54−25.70	RXC J2003.5−2323	20 03 32.3	−23 23 30	0.317	$7.5^{+0.6}_{-0.7}$	1.24	halo	0.7	47
G053.42−36.25	MACS J2135.2−0102	21 35 10.1	−01 03 15	0.330	$7.6^{+0.6}_{-0.6}$	1.24	no data	···	···
G055.95−34.87	A 2355	21 35 13.6	+01 25 40	0.231	$6.9^{+0.5}_{-0.5}$	1.24	no data	···	···
G073.98−27.83	A 2390	21 53 44.0	+17 41 35	0.233	$9.5^{+0.4}_{-0.4}$	1.38	halo	0.3	44
G073.85−54.94	A 2537	23 08 28.1	−02 12 00	0.297	$6.2^{+0.6}_{-0.7}$	1.17	no detection	···	6
G081.01−50.92	A 2552	23 11 36.3	+03 38 38	0.300	$7.5^{+0.6}_{-0.6}$	1.25	halo (c)	0.3	5
G087.03−57.37	A 2631	23 37 43.7	+00 16 06	0.278	$7.0^{+0.6}_{-0.6}$	1.23	no detection	···	6
G034.03−76.59	A 2667	23 51 38.3	−26 04 45	0.226	$6.8^{+0.5}_{-0.5}$	1.24	minihalo	0.05	2
Clusters without *Chandra* observations									
G092.10−66.02	A 2697	00 03 05.5	−06 05 26	0.232	$6.0^{+0.6}_{-0.6}$	1.19	no detection	···	8
G110.08−70.23	A 56	00 34 01.6	−07 47 45	0.300	$6.2^{+0.7}_{-0.7}$	1.17	no data	···	···
G114.34−60.16	RXC J0034.4+0225	00 34 23.6	+02 25 14	0.350	$6.5^{+0.7}_{-0.8}$	1.17	no data	···	···
G142.18−53.27	A 220	01 37 22.0	+07 52 31	0.330	$6.7^{+0.8}_{-0.9}$	1.19	no data	···	···
G222.97−65.69	A 3041	02 41 27.6	−28 38 51	0.232	$6.1^{+0.5}_{-0.6}$	1.19	no data	···	···
G205.07−62.94	···	02 46 27.6	−20 32 05	0.310	$7.4^{+0.6}_{-0.7}$	1.24	no detection	···	48
G176.25−52.57	A 384	02 48 13.1	−02 14 21	0.236	$6.4^{+0.6}_{-0.6}$	1.21	no data	···	···
G172.93+21.31	···	07 07 37.2	+44 19 23	0.331	$6.1^{+0.8}_{-0.8}$	1.15	no data	···	···
G169.64+33.84	···	08 16 42.5	+49 31 48	0.347	$6.2^{+0.8}_{-0.9}$	1.15	no data	···	···

Table 1 continued

Table 1 *(continued)*

Planck name PSZ1	Alternative name	RA_{J2000} (h,m,s)	DEC_{J2000} (deg, ′,″)	z	M_{500} (10^{14} $M_\odot$)	R_{500} (Mpc)	Central diffuse radio emission	R_{radio}/R_{500}	Radio reference
G227.55+54.88	ZwCl 1028.8+1419	10 31 21.1	+14 06 19	0.305	$6.1^{+0.7}_{-0.7}$	1.16	no data	···	···
G288.26+39.94	RXC J1203.2−2131	12 03 14.4	−21 33 02	0.192	$7.3^{+0.5}_{-0.5}$	1.28	no data	···	···
G304.76+69.84	···	12 53 58.8	+06 58 40	0.346	$6.2^{+0.7}_{-0.8}$	1.15	no data	···	···
G309.46+37.32	RXC J1314.4−2515	13 14 23.1	−25 15 09	0.244	$6.2^{+0.7}_{-0.7}$	1.19	halo	0.3	8,49
G068.32+81.81	RXC J1322.8+3138	13 22 48.0	+31 39 06	0.308	$6.6^{+0.6}_{-0.6}$	1.19	no data	···	···
G019.12+31.23	···	16 36 29.4	+03 08 51	0.280	$7.1^{+0.6}_{-0.7}$	1.23	no data	···	···
G049.83−25.22	RXC J2051.1+0216	20 51 20.3	+02 16 40	0.321	$6.1^{+0.7}_{-0.7}$	1.15	no data	···	···
G084.20−35.49	A 2472	22 42 20.6	+17 29 17	0.314	$6.2^{+0.7}_{-0.8}$	1.16	no data	···	···

NOTE— Column 1: *Planck* cluster name. Column 2: alternative name. Columns 3–6: cluster coordinates, redshift and mass from Planck collaboration et al. (2014). Column 7: R_{500}, derived from M_{500}. Column 8: type of diffuse radio emission at the cluster center (c indicates a candidate detection). As defined in §2, sources with $R_{radio} \leq 0.2R_{500}$ are classified as minihalos. Column 9: radius of the central diffuse radio source, as defined in §2, in units of R_{500}. Column 10: radio references. If more than one reference is given, the first one is the reference for the image used to measure the radio size. Reference code: (1) this work, (2) G17, (3) Govoni et al. (2001), (4) Venturi et al. (2013), (5) Kale et al. (2015), (6) Venturi et al. (2008), (7) Giovannini et al. (2009), (8) Venturi et al. (2007), (9) Kale et al. (2013), (10) Venturi et al., in preparation, (11) Bonafede et al., (private communication), (12) Bacchi et al. (2013), (13) Giacintucci et al. (2013), (14) Giacintucci et al. (2014a), (15) Brunetti et al. (2008), (16) Dallacasa et al.(2209), (17) Vacca et al. (2014), (18) Macario et al. (2014), (19) Giovannini & Feretti (2000), (20) Macario et al. (2011), (21) Macario et al. (2011), (22) Kassim et al. (2001), (23) Govoni et al. (2011), (24) Venturi et al. (2011a), (25) Gitti et al. (2006), (26) Doria et al. (2012), (27) Pandey-Pommier et al. (2016), (28) Reid et al. (1999), (29) Parekh et al. (2017), (30) Giacintucci et al. (2009a), (31) Bonafede et al. (2015), (32) Venturi et al. (2011b), (33) Macario et al. (2013), (34) Vacca et al. (2011), (35) Govoni et al. (2009), (36) Giacintucci et al. (2011a), (37) Giacintucci et al. (2011b), (38) Venturi et al. (2017), (39) Farnsworth et al. (2013), (40) Feretti et al. (2001), (41) Brentjens (2008), (42) Clarke & Ensslin (2006), (43) Giacintucci et al. (2014b), (44) Sommer et al. (2017), (45) Bonafede et al. (2014), (46) Kale & Parekh (2016), (47) Giacintucci et al. (2009b), (48) Ferrari et al., (private communication), (49) Feretti et al. (2005).

3.1. *Statistical sample*

A complete essentially mass-limited cluster sample can be extracted from the *Planck* SZ cluster catalog, since the cluster total SZ signal is a good proxy for the total mass (e.g., Nagai 2006). We selected all clusters with redshift $z \leq 0.35$, Galactic latitude $|b| \geq 20°$ and the *Planck*-estimated total mass within R_{500} of $M_{500} > 6 \times 10^{14}$ $M_\odot$. This mass cut is well above the *Planck* completeness limit and, along with the z cut, is a compromise between the need to cover a range of cluster masses and the availability of the radio and X-ray data. We also imposed a cut in declination of $DEC_{J2000} \geq -30°$ to ensure good visibility from the *VLA* and *GMRT*, whose observations we use to investigate the presence of diffuse radio emission at the cluster center. Finally, we excluded the double cluster A 115; its total mass inferred by *Planck* is 7.2×10^{14} $M_\odot$ (so above our mass limit), however, based on optical and X-ray estimates of the cluster mass ratio (Barrena et al. 2007; White et al. 1997), the mass of each individual cluster falls below our mass threshold.

Our final *Planck* sample contains 75 clusters, listed in Table 3. This is essentially the same sample, apart from slightly different selection criteria, as that used by Cuciti et al. (2015) to study the occurrence of giant radio halos in clusters. *Chandra* X-ray observations are currently available for 58 (77%) of these clusters; hereafter we will refer to these clusters as the *Chandra* statistical sample. 53 of these clusters (91%) have published accurate radio measurements from deep *Westerbork Synthesis Radio Telescope (WSRT)*, *VLA*, and/or *GMRT* observations (Table 3), most of the latter taken as part of the *GMRT* Radio Halo Survey and its extension (Venturi et al. 2007, 2008, Kale et al. 2013, 2015). Two of the remaining clusters — RXC J0510.7–0801 and RXC J0520.7–1328 — have pointed *GMRT* observations; however, the resulting images are not sensitive enough to investigate the presence of diffuse radio emission in these systems (Kale et al. 2015; Macario et al. 2014). We will see in §7 that these two clusters, along with those with no available radio data (A 1733, MACS J2135.2-0102 and A 2355), do not possess a cool core and the absence of radio information will not affect our main findings that are based on the cool-core part of the sample.

Our statistical sample (Table 3) contains 12 minihalos, of which 9 are previously known and three — A 2667, PSZ1 G139.61+24.2 (candidate) and RXC J1115.8+0129 (candidate) — are new detections. The former two are reported in the forthcoming paper G17 and the latter in Pandey-Pommier et al. (2016). The sample includes 26 radio-halo clusters and 5 candidates. Many of the clusters also contain peripheral radio relics, which is a distinct phenomenon (e.g., van Weeren et al. 2010) and we do not discuss it in this paper.

Among the 17 clusters in our *Planck* sample that do not have *Chandra* data (Table 3), 11 have *XMM-Newton* observations. However, most of them do not have high-sensitivity radio data at present. We inspected the *XMM-Newton* images and found that only 3 out of 11

can possibly have cool cores, thus omitting them does not significantly affect our statistical conclusions.

3.2. *Supplementary sample*

We supplement our statistical sample with additional 48 clusters drawn from ACCEPT, which includes clusters observed with *Chandra* as of 2008 and presents uniform X-ray analysis for them (C09), suitable for our work. The clusters were required to have deep, pointed *VLA*, *WSRT* and *GMRT* observations in the literature and/or in the data archives (see §6), be at $z \leq 0.5$, $\mathrm{DEC_{J2000}} \geq -30^{\circ}$ and an average temperature of $kT > 3.5$ keV. This temperature cut corresponds to a lower total mass ($\sim 2 \times 10^{14}\ M_{\odot}$, based on an $M_{500} - T_{\mathrm{X}}$ relation, Vikhlinin et al. 2009) than the lower limit of our statistical sample. To those clusters we add the Phoenix cluster ($z = 0.6$), which hosts the most distant minihalo found to date (van Weeren et al. 2014). This supplementary sample is given in Table 2. Twelve of these clusters possess a minihalo, including a recent *GMRT* detection in A907 (G17), and 4 host a candidate minihalo. The presence of a central diffuse radio source has been reported in 3 more clusters in this sample — ZwC 1742.1+3306, MACS J1931.8–2634 (Giacintucci et al. 2014a) and A 2626 (Gitti 2013) — but their classification as a minihalo is uncertain: the size (< 50 kpc in A 2626 and ZwC 1742.1+3306), radio morphology and ultra-steep spectrum ($\alpha_{\mathrm{radio}} \sim 2$) of these sources, as well as the possible association with X-ray cavities in MACS J1931.8–2634, suggest that they could instead be dying/restarted radio galaxies (Giacintucci et al. 2014a), whose aged emission, no longer fed by the central nucleus, is rapidly fading. For 9 clusters with no published radio results on the minihalo angular scales, we analyzed *VLA* archival observations (§6) and present the results here (no minihalos were detected among them).

Our final combined sample (statistical + supplementary) consists of 106 clusters and includes all 28 known minihalos, including 6 candidates.

Table 2. Supplementary Sample

Cluster name	Planck name PSZ1	$\mathrm{RA_{J2000}}$ (h,m,s)	$\mathrm{DEC_{J2000}}$ (deg, ′,″)	z	M_{500} ($10^{14}\ M_{\odot}$)	R_{500} (Mpc)	Central diffuse radio emission	$R_{\mathrm{radio}}/R_{500}$	Radio reference
Z348	···	01 06 50.3	+01 03 17	0.255	$2.5 \pm 0.3^{\star}$	0.88	no detection	···	3
A 119	G125.68−64.12	00 56 14.5	−01 16 55	0.044	$3.34^{+0.22}_{-0.23}$	1.04	no detection	···	4
A 141	G175.59−85.95	01 05 34.6	−24 38 00	0.230	$4.48^{+0.6}_{-0.73}$	1.08	no detection	···	3
A 193	G136.90−53.31	01 24 59.4	+08 38 43	0.049	$1.8^{+0.27}_{-0.29}$	0.85	no detection	···	1
A 267	G153.07−58.27	01 52 41.9	+00 58 01	0.227	$4.95^{+0.67}_{-0.72}$	1.11	no detection	···	3
MACS J0159.8-0849	G167.63−65.57	01 59 54.5	−08 50 14	0.405	$6.88^{+0.90}_{-0.98}$	1.16	minihalo	0.1	5, 2
A 383	G177.64−53.52	02 47 46.5	−03 29 56	0.188	$4.47^{+0.60}_{-0.64}$	1.09	no detection	···	1
A 399	G164.31−39.43	02 57 52.7	+13 04 11	0.072	$5.29^{+0.34}_{-0.35}$	1.20	halo	0.25	6
Perseus	···	03 19 47.2	+41 30 47	0.018	$6.1 \pm 0.6^{\star}$	1.28	minihalo	0.1	7, 8, 9
MACS J0329.6-0211	···	03 29 41.5	−02 11 46	0.450	$4.9 \pm 0.7^{\star}$	1.02	minihalo	0.1	2, 5
2A 0335+096	G176.30−35.06	03 38 44.4	+09 56 34	0.035	$2.27^{+0.24}_{-0.25}$	0.92	minihalo	0.1	2, 10
MACS J0417.5-1154	G205.94−39.46	04 17 36.2	−11 54 12	0.443	$11.70^{+0.64}_{-0.66}$	1.37	halo	0.3	11
MACS J0429.6-0253	···	04 29 36.0	−02 53 08	0.399	$4.1 \pm 0.8^{\star}$	0.98	no detection	···	1
RX J0439.0+0715	G189.52−25.10	04 39 01.2	+07 15 36	0.244	$5.75^{+0.70}_{-0.74}$	1.16	no detection	···	3
MS 0440.5+0204	···	04 43 09.7	+02 10 19	0.190	$5.0 \pm 1.2^{\star}$	1.13	no detection	···	1
A 611	G184.70+28.92	08 01 01.7	+36 05 06	0.288	$5.85^{+0.60}_{-0.64}$	1.15	no detection	···	4
MS 0839.8+2938	···	08 42 55.9	+29 27 26	0.194	$3.4 \pm 0.5^{\star}$	1.00	no detection	···	1
Z 2089	···	09 00 37.9	+20 54 58	0.235	$3.2 \pm 0.4^{\star}$	0.96	no detection	···	3, 4
ZwCl 2701	···	09 52 49.2	+51 53 05	0.214	$4.0 \pm 0.5^{\star}$	1.04	no detection	···	3, 4
A 907	G249.38+33.27	09 58 22.2	−11 03 35	0.167	$5.18^{+0.47}_{-0.50}$	1.16	minihalo	0.05	2
ZWCL 3146	···	10 23 39.6	+04 11 10	0.291	$6.7 \pm 0.8^{\star}$	1.20	minihalo	0.07	12, 5
A 1068	G179.13+60.14	10 40 48.7	+39 56 05	0.137	$3.55^{+0.38}_{-0.41}$	1.03	minihalo (c)	0.10	13

Table 2 continued

Table 2 *(continued)*

Cluster name	Planck name PSZ1	RA_{J2000} (h,m,s)	DEC_{J2000} (deg, ′,″)	z	M_{500} (10^{14} $M_\odot$)	R_{500} (Mpc)	Central diffuse radio emission	R_{radio}/R_{500}	Radio reference
A 1204	···	11 13 32.2	+17 35 40	0.171	$2.4 \pm 0.3^\star$	0.89	no detection	···	1
A 1240	···	11 23 32.1	+43 06 32	0.159	$2.6 \pm 0.4^\star$	0.92	no detection	···	14
A 1413	G226.19+76.78	11 55 19.4	+23 24 26	0.143	$5.98^{+0.38}_{-0.40}$	1.22	minihalo (c)	0.09	13
A 1576	G125.72+53.87	12 36 48.9	+63 10 40	0.302	$5.98^{+0.48}_{-0.50}$	1.16	no detection	···	3
A 1650	G306.71+61.04	12 58 45.6	−01 46 11	0.085	$4.00^{+0.34}_{-0.36}$	1.09	no detection	···	13
RX J1347.5–1145	G324.05+48.79	13 47 33.5	−11 45 42	0.452	$10.61^{+0.74}_{-0.77}$	1.32	minihalo	0.2	2, 15, 16
A 1795	G033.84+77.17	13 48 55.0	+26 36 01	0.062	$4.54^{+0.21}_{-0.21}$	1.15	minihalo (c)	0.09	5
A 1995	G096.87+52.48	14 52 56.4	+58 03 35	0.318	$5.15^{+0.49}_{-0.52}$	1.09	halo	0.3	17
MS 1455.0+2232	···	14 57 15.1	+22 20 34	0.258	$3.46 \pm 0.35^\star$	0.98	minihalo	0.1	2, 4, 18
A 2034	G053.52+59.52	15 10 12.6	+33 29 21	0.113	$4.92^{+0.35}_{-0.36}$	1.16	halo	0.3	17
RX J1532.9+3021	···	15 32 53.8	+30 20 58	0.363[a]	$4.7 \pm 0.6^\star$	1.04	minihalo	0.10	5, 3, 19
A 2111	G054.99+53.42	15 39 34.9	+34 25 46	0.229	$5.46^{+0.60}_{-0.64}$	1.15	no detection	···	4
A 2125	···	15 40 58.3	+66 18 28	0.247	$1.6 \pm 0.3^\star$	0.76	no detection	···	1
Ophiuchus	···	17 12 25.9	−23 22 33	0.028	$12.4 \pm 1.2^\star$	1.62	minihalo	0.15	2, 13, 20
A 2255	G093.93+34.92	17 12 48.4	+64 04 03	0.081	$5.19^{+0.19}_{-0.19}$	1.19	halo	0.7	21, 22, 23
RX J1720.2+3536	G059.51+33.06	17 20 20.6	+35 37 42	0.387	$6.04^{+0.69}_{-0.74}$	1.12	minihalo (c)	0.18	24
ZwCl 1742.1+3306	G057.91+27.62	17 44 19.6	+32 59 19	0.076	$2.63^{+0.27}_{-0.29}$	0.95	uncertain	0.04	5
A 2319	G075.71+13.51	19 21 09.6	+43 58 30	0.056	$8.59^{+0.22}_{-0.22}$	1.42	halo	0.4	25, 26, 27
MACS J1931.8-2634	G012.58−20.07	19 31 46.0	-26 33 51	0.352	$6.19^{+0.77}_{-0.83}$	1.15	uncertain	0.1	5, 28
RX J2129.6+0005	G053.65−34.49	21 29 42.5	+00 04 51	0.235	$4.24^{+0.55}_{-0.59}$	1.06	minihalo	0.08	12, 2
A 2420	G046.48−49.42	22 10 12.9	−12 09 51	0.085	$4.48^{+0.26}_{-0.27}$	1.13	no detection	···	1
MACS J2228.5+2036	G083.30−31.01	22 28 29.1	+20 38 22	0.412	$7.82^{+0.71}_{-0.75}$	1.21	no detection	···	4, 11
MACS J2245.0+2637	···	22 45 04.7	+26 38 04	0.304	$4.8 \pm 0.8^\star$	1.07	no detection	···	29
A 2556	···	23 13 00.9	−21 37 55	0.087	$2.4 \pm 0.2^\star$	0.92	no detection	···	1
A 2626	···	23 36 30.3	+21 08 33	0.055	$2.4 \pm 0.5^\star$	0.93	uncertain	0.03	30
Phoenix[b]	···	23 44 42.2	−42 43 08	0.597	$12.6^{+2.0}_{-1.5}$	1.32	minihalo	0.17	31

[a] Crawford et al. (1999).

[b] SPT-CL J2344-4243: coordinates, redshift and mass are from McDonald et al. (2015) and references therein.

NOTE—Column 1: cluster name. Column 2: *Planck* name. Columns 3–5: cluster coordinates and redshift from Planck collaboration et al. (2014) for the *Planck* clusters and NASA/IPAC Extragalactic Database for the others. Column 6: cluster mass from Planck collaboration et al. (2014). Values marked with * were estimated from the $M_{500} - T_X$ relation of Vikhlinin et al. (2009) using the core-excised temperatures in Table 6; errors were calculated from the temperature uncertainties and include statistical and systematic uncertainties for the $M_{500} - T_X$ relation itself (§4). Column 8: R_{500}, derived from M_{500}. Column 7: type of diffuse radio emission at the cluster center (c indicates a candidate detection). As defined in §2, sources with $R_{radio} \leq 0.2R_{500}$ are classified as minihalos. Clusters marked as *uncertain* host central extended radio sources whose classification as a minihalo is uncertain; the radio size, morphology and ultra-steep spectrum of these sources suggest that they could be instead dying/restarted radio galaxies (§3.2; Giacintucci et al. 2014a). Column 9: radius of the central diffuse radio source, as defined in §2, in units of R_{500}. Column 10: Radio references. If more than one reference is given, the first one is the reference for the image used to measure the radio size. Reference code: (1) this work, (2) G17, (3) Kale et al. (2013), (4) Venturi et al. (2008), (5) Giacintucci et al. (2014a), (6) Murgia et al. (2010a), (7) Sijbring (1993), (8) Burns et al. 1992, (9) Gendron-Marsolais et al. (2017), (10) Sarazin et al. (1995), (11) Parekh et al. (2017), (12) Kale et al. (2015), (13) Govoni et al. (2009), (14) Bonafede et al. (2009), (15) Gitti et al. (2007), (16) Ferrari et al. (2011), (17) Giovannini et al. (2009), (18) Mazzotta & Giacintucci (2008), (19) Hlavacek-Larrondo et al. (2013), (20) Murgia et al. (2010b), (21) Pizzo & de Bruyn (2009), (22) Govoni et al. (2005), (23) Feretti et al. (1997a), (24) Giacintucci et al. (2014b), (25) Storm et al. (2015), (26) Farnsworth et al. (2013), (27) Feretti et al. (1997b), (28) Ehlert et al. (2011), (29) Venturi et al., in preparation, (30) Gitti (2013), (31) van Weeren et al. (2014).

4. CLUSTER X-RAY PROPERTIES

The purpose of this study is to quantify the occurrence of radio minihalos in clusters of different total masses with and without cool cores. To identify cool-core clusters in the sample, we follow C09 and use the specific entropy "floor" in the cluster centers. They find that the radial dependence of the specific entropy, defined in C09 and here as

$$K \equiv kTn_e^{-2/3}, \quad (1)$$

where T is the gas temperature and n_e is the electron number density, can be described, in the cluster central regions, as a function of radius, r, by

$$K(r) = K_0 + K_{100}\left(\frac{r}{100\,\mathrm{kpc}}\right)^\alpha \quad (2)$$

where K_0 is the so-called core entropy, K_{100} is a normalization for entropy at 100 kpc, and α is the power-law index.

Clusters with $K_0 < 30 - 50$ keV cm^2 (which represents a deep minimum of the entropy at the cluster center) invariably exhibit all the attributes of a cool core. For the cluster entropy profiles in the ACCEPT database, C09 combined projected gas temperatures with 3-dimensional gas densities, which does not yield physically meaningful entropy values. However, their values serve our current purpose of identifying the cool cores well, and have been used for similar purposes in the literature. Therefore, for the present analysis, we chose to use the K_0 values from C09 for those clusters that already had high-quality *Chandra* data (81 out of 106 clusters in our combined sample), and emulate the C09 derivation (with some technical differences) for the 27 clusters with new or significantly-improved *Chandra* data that appeared since C09. This will be described in §5.5.

For cluster total masses, we use the *Planck* SZ-based estimates where available, otherwise we obtain a mass estimate from the $M_{500} - T_{\rm X}$ relation in Vikhlinin et al. (2009), using an X-ray measured, core-excised temperature. $M_{500} - T_{\rm X}$ estimates are required for 17 out of 48 clusters (35%) in the supplementary sample. Core-excised temperatures are taken from Cavagnolo et al. (2008, hereafter C08) if available, otherwise we derive them here (§5.4) in the same manner for uniformity. Errors for those masses are calculated from the temperature statistical uncertainties and include statistical and systematic uncertainties for the $M_{500} - T_{\rm X}$ relation itself, as estimated by Vikhlinin et al. (2009).

5. *CHANDRA* DATA ANALYSIS

The ACCEPT sample of C09 contains clusters in the *Chandra* archive as of 2008. Since then, *Chandra* observed new clusters, e.g., those in our statistical sample that were discovered by *Planck* (2 clusters), and reobserved others, including several borderline clusters ("warm cores") for which it is important for us to have an accurate core temperature profile. Here, we have analyzed *Chandra* data for such new clusters and important improvements. Seven of the new observations are part of the *Chandra* Visionary Program to study the X-ray properties of *Planck*-selected clusters, including the fraction of cool cores (Andrade-Santos et al. 2017).

We will use C08 and C09 entropy and temperature values for those clusters that have been reobserved but for which the old data were accurate enough. Updates of *Chandra* calibration since C08 and C09 have negligible effects for our current qualitative purposes.

5.1. *Data reduction and image preparation*

The *Chandra* observations analyzed in this paper are listed in Table 3, which includes the observation identifiers, clean exposure times and the adopted Galactic absorption column density N_H (§5.3). The Level-1 ACIS event files from the archive were reprocessed following the procedure described in Vikhlinin et al. (2005) using the *Chandra* Calibration Database (CALDB) 4.6.3. Exclusion of time intervals with elevated background and background modeling were done as described in Markevitch et al. (2003). To model the detector and sky background, we used the blank-sky datasets from the CALDB appropriate for the date of each observation, normalized using the ratio of the observed to blank-sky count rates in the 9.5–12 keV band. Following Markevitch et al. (2000), we also subtracted the ACIS readout artifact, which is an important effect on the radial temperature profiles in the presence of a sharp brightness peak.

We used images in the 0.5–4 keV and 2–7 kev energy bands to detect the unrelated X-ray point sources and small-scale extended sources in each observation. These sources were masked from the image and spectral analysis. For each cluster, we need to extract and fit a radial surface brightness profile and a radial temperature profile.

Table 3. *Chandra* observations analyzed in this work

Cluster name	Observation ID	Detector (ACIS)	Exposure (ksec)	N_H (10^{20} cm^{-2})
A 2813	9409	I	20.0	1.84*
A 2895	9429	I	19.7	1.37*
RXC J0142.0+2131	10440	I	20.0	6.20*
A 401	14024	I	111.5	$13.04^{+0.30}_{-0.30}$

Table 3 continued

Table 3 *(continued)*

Cluster name	Observation ID	Detector (ACIS)	Exposure (ksec)	N_H (10^{20} cm^{-2})
A 3088	9414	I	19.2	$1.27^{\star}$
PSZ1 G171.96-40.64	15302	I	25.9	$31.69^{+1.59}_{-1.57}$
RXC J0510.7-0801	14011	I	20.7	$6.44^{\star}$
PSZ1 G139.61+24.20	15139,15297	I, I	17.9,9.3	$13.11^{+1.7}_{-1.6}$
A 781	15128	I	33.7	$1.65^{\star}$
A 3444	9400	S	36.3	$5.55^{\star}$
A 1132	13376	I	9.1	$8.52^{+1.9}_{-1.6}$
A 1351	15136	I	32.9	$0.98^{\star}$
A 1423	11724	I	25.7	$1.81^{\star}$
A 1443	16279	I	18.9	$5.18^{+1.9}_{-1.4}$
RXC J1234.2+0947	11727	I	20.7	$1.61^{\star}$
A 1682	11725	I	19.7	$1.04^{\star}$
A 1689	6930, 7289	I, I	76,75	$3.48^{+0.29}_{-0.29}$
A 1733	11771	I	6.7	$1.81^{\star}$
AS 780	9428	S	39.4	$7.39^{\star}$
RXC J1504.1–0248	17197,17669,17670	I, I, I	29.8,28.5,44.6	$14.35^{+4.6}_{-4.6}$
RXC J1514.9-1523	15175	I	59.1	$8.28^{\star}$
A 2142	5005,15186	I, S	39.4,87.1	$6.16^{+0.12}_{-0.12}$
CL 1821+643	9398	S	34.2	$3.44^{\star}$
RXC J2003.5-2323	7916	I	50.0	$7.57^{\star}$
MACS J2135.2-0102	11710	I	26.9	$3.88^{\star}$
A 2355	15097	I	14.5	$8.98^{+2.41}_{-2.18}$
A 2552	11730	I	22.8	$4.60^{\star}$
A 2667	2214	S	9.3	$1.73^{\star}$
Z348	10465	S	48.7	$2.50^{\star}$
A 141	9410	I	19.7	$1.79^{\star}$
Z2089	10463	S	40.4	$2.88^{\star}$
A 1240	4961	I	51.8	$2.85^{\star}$
A 1413	5002	I	37.1	$1.83^{\star}$
A 1576	15127	I	28.8	$1.08^{\star}$
A 1650	7242	I	37.6	$1.35^{\star}$
ZwCl 1742.1+3306	8267	I	7.8	$3.83^{\star}$
RX J2129.6+0005	9370	I	29.8	$3.64^{\star}$
A 2420	8271	I	7.8	$3.70^{\star}$
A 2626	3192	S	24.9	$3.83^{\star}$
Phoenix	16545	I	59.9	$1.52^{\star}$

NOTE— Column 1: cluster name. Column 2: observation identification number. Column 3: *Chandra* ACIS detector. Column 4: Total clean exposure. Column 5: Galactic absorption column density adopted in this paper; values marked with * are from LAB (§5.3).

5.2. *Gas density profiles*

For each cluster, we obtained a background-subtracted, exposure-corrected image in the 0.7–2 keV band. For clusters with multiple (typically offset) ACIS observations, we first coadded the individual background-subtracted images and then divided the counts images by the sum of the corresponding exposure maps. We then extracted radial surface brightness profiles, centered on the cluster X-ray centroid.

While a simple spherically-symmetric β-model for the gas density (Cavaliere & Fusco-Femiano 1978) is a reasonable description for non-cool-core clusters, it does not describe cool cores well (e.g., Jones & Forman 1984). We therefore fit the brightness profiles by projecting a

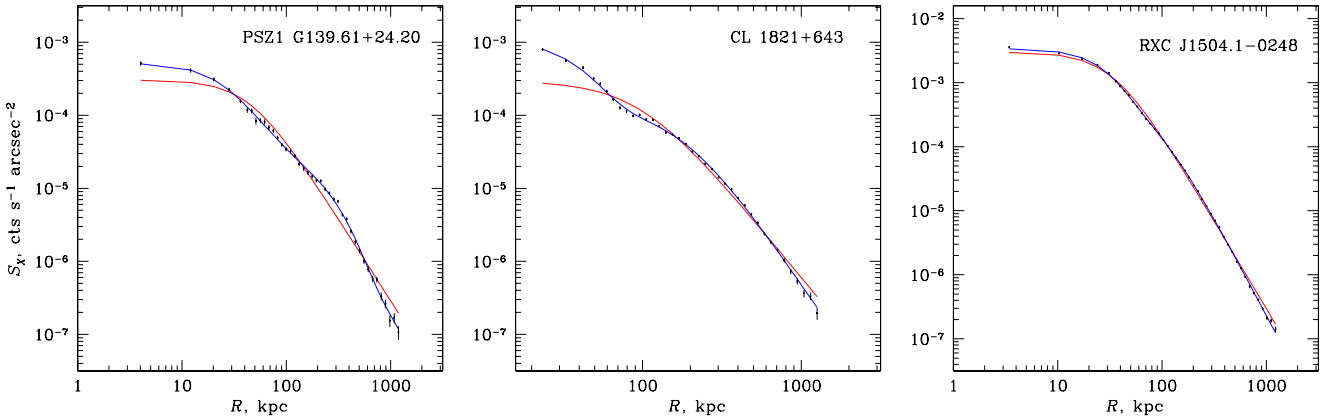

Figure 1. *Chandra* X-ray surface brightness profiles of PSZ1 G139.61+24.20, CL 1821+643 and RXC J1504.1-0248. Solid lines show the best-fit single (red) and double (blue) β-models.

spherically-symmetric double β-model,

$$n_e(r) = \frac{n_0}{1+f}\left[\left(1+\frac{r^2}{r_{c1}^2}\right)^{-\frac{3}{2}\beta_1} + f\left(1+\frac{r^2}{r_{c2}^2}\right)^{-\frac{3}{2}\beta_2}\right], \quad (3)$$

where n_0 (central density for the sum of the two components), r_{c1}, r_{c2}, β_1, β_2, and f were free parameters. We ignore the very mild temperature dependence of the X-ray emissivity in this *Chandra* band and the relevant range of temperatures. Fits to the brightness profile were done out to R_{500} or as far in radius as the *Chandra* coverage allowed, which in all cases was far beyond the cores. While such a model is not physically motivated (and no physical significance should be assigned to the particular values of r_c and β), it fits all our clusters well, which is what we need for determining the central entropy. For those clusters where a single β-model provided a good fit, we set $f = 0$. Example cool-core fits with single and double β-models are shown in Fig. 1, and fit results for all clusters are given in Table 4. We do not derive errors on best-fit quantities, because statistical errors are negligible and uncertainties of the geometry dominate. The entropy uncertainties will be dominated by the temperature accuracy.

5.3. *Spectral analysis*

We derived the intracluster medium temperatures using the *Chandra* data as follows. For each observation, we extracted a spectrum of the cluster for each region of interest, and generated the instrument responses (ARF and RMF) using the current calibration files (version N0008 for the telescope effective area, N0006 for the CCD quantum efficiency, and N0009 for the ACIS time-dependent low-energy contamination model).

The background spectra were extracted for the same regions from the corresponding blank-sky datasets, normalized as in §5.1. To ensure the sky-variable soft cosmic X-ray background is subtracted correctly, we checked for the presence of significant excess/deficit of soft X-ray thermal emission in the spectrum using local background regions. In those cases where significant systematic residuals were found, they were modeled with a low-temperature APEC or absorbed power-law and then included as a fixed additional background component in the spectral fits, normalized by the region area, as in Vikhlinin et al. (2005). This has little effect in the cores, but affects the fits in the outskirts.

The cluster X-ray emission was modeled with an absorbed, single-temperature APEC model in the the 0.7–7 keV energy band, with the metal abundance free to vary. For the full-cluster spectra, the absorption column density N_H was allowed to vary. If the best-fit N_H value was consistent with that from the Leiden/Argentine/Bonn (LAB) radio survey of Galactic HI (Kalberla et al. 2005), we fixed it at the database value for subsequent analysis. The adopted N_H values are listed in Table 3

For several clusters, we combined multiple *Chandra* observations (Table 3) by fitting their spectra simultaneously with the temperature and metal abundance of the hot APEC components tied together. For RXC J1504.1-0248, for which the observations had the same pointing position and roll angle and thus had the same responses, we instead coadded the spectra.

Table 4. Gas density profile β-model fits

Cluster name	n_0 (10^{-3} cm^{-3})	r_{c1} (kpc)	β_1	r_{c2} (kpc)	β_2	f
A 2895	5.6	212	0.7	...	...	0
RXC J0142.0+2131	16.1	32	0.6	212	0.7	0.50
A 401	8.6	51	0.3	277	1.1	0.65
PSZ1G171.96-40.64	11.4	183	3.0	376	0.8	0.73
RXC J0510.7-0801	8.9	143	1.2	647	1.1	0.40
PSZ1 G139.61+24.20	77.3	22	0.5	804	3.0	0.03
A 781	4.2	237	2.3	644	0.9	0.66
A 3444	77.9	37	0.7	190	0.6	0.07
A 1132	4.3	256	0.7	...	...	0
A 1351	3.0	683	1.4	...	...	0
A 1423	18.5	56	0.6	422	0.6	0.05
A 1443	4.3	276	0.6	...	...	0
RXC J1234.2+0947	1.6	549	0.8	...	...	0
A 1682	6.4	156	3.0	329	0.8	0.81
A 1689	34.3	123	3.0	184	0.7	0.44
A 1733	5.1	176	0.6	...	...	0
AS 780	86.5	21	0.5	...	...	0
RXC J1504.1−0248	170.2	68	3.0	75	0.7	0.41
RXC J1514.9−1523	2.0	592	0.8	...	...	0
A 2142	27.6	90	3.0	139	0.6	0.81
CL 1821+643	80.5	86	3.0	186	0.7	0.18
RXC J2003.5−2323	2.2	698	1.0	...	...	0
MACS J2135.2−0102	5.6	191	0.6	...	...	0
A 2355	2.1	615	1.0	...	...	0
A 2552	18.1	54	0.7	238	0.7	0.40
Z348	75.2	33	0.7	...	...	0
Phoenix	209.4	34	0.6	...	...	0

NOTE—Column 1: cluster name. Columns 2–7: parameters of a β-model fit, see eq. (3). Fits were done out to R_{500} or as far in radius as the *Chandra* coverage allowed, which in all cases was far beyond the core region.

5.4. *Average cluster temperatures*

One of the quantities that we correlate with the presence of a radio halo is the global cluster temperature. In addition, for those clusters in the supplementary sample that do not have *Planck* masses, we estimate total masses from the $M_{500} - T_{\rm X}$ relation (§4). For 29 clusters in the statistical sample and for most in the supplementary one, we used core-excised global temperatures from C08. For the remaining clusters in the supplementary sample and for 12 in the statistical one with significantly better recent *Chandra* observations, we derived global temperatures (§5.3) using a spectrum extracted from an annulus with 70 kpc$< r < R_{2500}$[5] as in C08. The core-excised temperatures, $T_{\rm X,\,ce}$, of all clusters are summarized in Tables 6 and 7. The exceptions are 2A0335+096, Perseus and Ophiuchus, for which we used average temperatures from *ASCA*[6] because of *Chandra*'s limited radial coverage. Another nearby cluster for which we used the total temperature from the literature is A193, a clear non-cool-core cluster, for which core excision would not change the temperature significantly. For cool cores, this should result in slightly underestimated masses from the $M_{500} - T_{\rm X}$ relation. This will not affect our qualitative conclusions.

[5] R_{2500} is the radius that encloses a mean overdensity of 2500 with respect to the critical density at the cluster redshift.

[6] *Advanced Satellite for Cosmology and Astrophysics.*

Table 5. Best-fit parameters for temperature and entropy profiles

Cluster name	T_0 (keV)	r_t (Mpc)	a	$T_{\rm min}/T_0$	$r_{\rm cool}$ (kpc)	$a_{\rm cool}$	K_0 (keV cm^2)	K_{100} (keV cm^2)	α	$r_{\rm max}$ (Mpc)
A 2895	11.1	0.3	−0.3	1.0*	...	...	173 ± 65	106	1.0	1.4
RXC J0142.0+2131	7.5	1.9	0.0*	1.0*	...	...	131 ± 51	90	1.2	1.8
A 401	7.9	3.1	0.0*	1.0*	...	...	180 ± 6	82	1.3	1.0
PSZ1G171.96−40.64	11.6	0.9	0.0*	1.0*	...	...	329 ± 74	42	1.4	2.0
RXC J0510.7−0801	9.2	1.0	0.0*	1.0*	...	...	158 ± 99	129	0.9	1.0
PSZ1 G139.61+24.20	13.8	0.4	0.0*	0.04	62	0.8	10 ± 10	186	1.1	0.1
A 781	8.2	1.0	0.0*	1.0*	...	...	$170 \pm 36^{(a)}$	196	0.7	1.8
A 3444	12.6	0.8	0.0*	0.31	299	1.1	18 ± 2	100	1.3	0.5
A 1132	9.5	0.4	−0.33	1.0*	...	...	$154 \pm 31^{(a)}$	111	0.9	1.1
A 1351	13.4	0.6	0.0*	1.0*	...	...	620 ± 93	3	2.6	1.3
A 1423	9.7	0.6	−0.28	1.0*	...	...	27 ± 18	170	1.0	1.2
A 1443	8.7	5.0	0.0*	1.0*	...	...	$283 \pm 57^{(a)}$	61	1.4	1.6
RXC J1234.2+0947	6.5	0.9	0.0*	1.0*	...	...	404 ± 93	23	1.3	1.2
A 1682	10.4	0.4	−0.37	1.0*	...	...	$143 \pm 26^{(a)}$	139	1.0*	1.1
A 1689	13.0	0.6	−0.16	1.0*	...	...	59 ± 4	109	1.7	0.1
AS 780	9.5	5.8	0.0*	0.37	146	3.2	19 ± 2	110	1.7	0.2
RXC J1504.1−0248	19.2	0.4	0.0*	0.15	348	1.0	11.1 ± 0.3	86	1.6	0.2
RXC J1514.9−1523	11.4	0.8	−0.10	1.0*	...	...	$490 \pm 108^{(a)}$	52	1.2	0.8
A 2142	12.8	1.3	−0.21	1.0*	...	...	58 ± 2	127	1.2	1.0
CL 1821+643	9.5	5.0	0.0*	0.38	88	4.2	8 ± 5	125	1.3	0.2
RXC J2003.5−2323	17.6	0.4	0.0*	1.0*	...	...	708 ± 85	11	1.3*	1.1
MACS J2135.2-0102	12.4	0.7	−0.32	1.0*	...	...	142 ± 18	145	1.0	1.9
A 2355	10.5	1.4	0.0*	1.0*	...	...	519 ± 117	57	1.3*	0.8
A 2552	12.8	0.7	−0.21	1.0*	...	...	78 ± 33	164	1.0	1.6
Z348	4.7	0.6	0.0*	0.53	95	2.6	13 ± 1	73	1.7	0.2
Phoenix	32.6	0.4	0.0*	0.21	255	1.5	19 ± 3	123	1.7	0.3

[a] uncertainty from error in the first bin of the temperature profile.

[⋆] fixed in the fit.

NOTE—Column 1: cluster name. Columns 2–7: best-fit parameters of the temperature fit, see eq. (4). Columns 8–10: best-fit parameters of the entropy fit (see §5.5 for details). Column 11: maximum radius used for the entropy fit.

5.5. *Temperature and specific entropy profiles*

We obtained radial temperature profiles by fitting spectra in annuli centered on the X-ray surface brightness peak or the centroid for disturbed clusters without a well-defined peak. The radial bins were selected as a compromise between the need to sample well the temperature decline in the cores and to keep the uncertainties small. The maximum radius was as far as the detector coverage and the background uncertainties allowed; this is unimportant as we are interested in the cores. The spectra were fit as described in §5.4, with metallicities allowed to vary at small radii (since we expect strong gradients in cool cores) and fixed at 0.2 solar at large radii. The N_H was fixed at the full-cluster values given in Table 3. The resulting projected temperature profiles for the clusters analyzed in this work are shown in Figs. 2–6, except for A 1733, which only has a 7 ks *Chandra* exposure (see below).

Our goal here is to derive the specific entropy floor in cluster centers, defined in the same way as in C09 (§4). For this purpose, we take our best-fit 3D density profile in the form of eq. (3), assume the entropy radial dependence given by eq. (2), calculate a temperature at a given radius from eq. (1). These temperature values are then averaged within each radial bin of the measured temperature profiles using the weighting of Mazzotta et al. (2004). The average values are compared with the observed temperature profiles, and the parameters K_0, K_{100} and α are fit in such a way. Because of limited modeling freedom of eq. (2), such a temperature profile usually described the cool cores well but often not the regions outside the core. Therefore, we only used the radii where it fit well, similarly to C09.

The modeled projected temperature profiles are shown as blue lines overlaid on the measured profiles in Figs. 2–6, and the best-fit entropy profile parameters, as well as the maximum radius used for the fit, are given in Table 5. For A 1733, the central entropy is estimated using the best-fit density profile and the temperature within the central $r = 120$ kpc region, which is enough to determine that it is not a cool core (Table 6).

For reference in our future work, and to verify the above model, we also fit the observed temperature profiles with a more complex phenomenological 3D temperature model used by Vikhlinin et al. (2006):

$$T(r) = T_0\, t_{\rm cool}(r)\, t(r), \tag{4}$$

where

$$t(r) = \left(\frac{r}{r_t}\right)^{-\alpha} \left[1 + \left(\frac{r}{r_t}\right)^{b}\right]^{-c/b} \tag{5}$$

describes the temperature profile outside the central cooling region and

$$t_{\rm cool}(r) = \frac{x + T_{\rm min}/T_0}{x+1},\ x \equiv \left(\frac{r}{r_{\rm cool}}\right)^{a_{\rm cool}} \tag{6}$$

describes the temperature decline in the central region. T_0, r_t, α, b, c, $r_{\rm cool}$, $a_{\rm cool}$ and $T_{\rm min}$ are free parameters. The term $t_{\rm cool}(r)$ was required only in several cases with a strong radial increase of the temperature profile in the core; in most cases, setting $t_{\rm cool}(r) \equiv 1$ was sufficient for a good fit, as the term $t(r)$ alone can describe a temperature dip in the center. We also fixed $b = 2$ and $c = 1$, which provides a good fit in all cases. The model was projected along the line of sight and within each radial bin and fit to the observed projected temperature profiles. The best-fit profile parameters are given in Table 5. The 3D and the corresponding projected profiles are shown by red curves (dashed and solid, respectively) in Figs. 2–6. Because this model is more flexible, it can describe the whole radial range of the measured temperatures. Comparison with the profiles for the entropy model (blue lines) shows that the entropy model provides an adequate temperature fit in the cores of all clusters.

Because we will combine the central entropy values from C09 and from our new analysis, we checked their consistency using RXJ1504.1–0248, one of the clusters in the C09 sample for which we used a more recent *Chandra* dataset. Our best-fit central density (from a double β-model fit, see Fig. 1) is only 7% higher than that in C09 (who derived it using the deprojection method), and our entropy floor value of $K_0 = 11.1 \pm 0.3$ keV cm^2 is consistent with, and more accurate than, the C09 value of $K_0 = 13 \pm 1$ keV cm^2. Other parameters of the core entropy profile are in agreement as well. The accuracy of K_0 depends on the number of temperature bins in the core, which is where the new data helped.

6. RADIO ANALYSIS

We analyzed *VLA* archival observations at 1.4 GHz of those clusters in our supplementary sample with no high-sensitivity and multi-resolution radio images on the minihalo angular scales in the literature (9 clusters). The observations were chosen to be suitable to search for diffuse radio emission on the cluster core scale, i.e., deep and with a good sampling of the *uv*–plane, particularly at short spacings, that are crucial to properly image extended, low surface brightness radio emission. Furthermore, we selected observations with a range of angular resolutions that allow us to discriminate between genuine diffuse emission and a blend of individual radio galaxies, as well as to separate a possible minihalo from the radio source associated with the cluster central galaxy.

Here we provide a brief description of the data reduction. The observation details, radio images and notes on the individual clusters are presented in Appendix A. The data were calibrated and reduced in the standard fashion using the NRAO Astronomical Image Processing System (AIPS) package. Self-calibration was applied to reduce the effects of residual phase and amplitude errors in the data and improve the quality of the final images. For each cluster, the observations in different array configurations were processed and imaged separately. When possible, data from different dates and configurations were combined together in the *uv* or image plane. Sets of images were produced with different weighting schemes, ranging from pure uniform weighting (Briggs "robustness" parameter (Briggs 1995) *ROBUST*$= -5$) to natural weighting (*ROBUST*$= +5$), to enhance any possible extended emission. The flux density scale was set using the Perley & Butler (2013) coefficients, and residual amplitude errors are within 3–5%.

No new minihalos were detected among the 9 clusters analyzed here. As an illustrative example, in Fig. 7 we show a comparison between a known minihalo (in our statistical sample) and two non-detections based on our radio analysis. Panel *a* shows the minihalo in the cool-core cluster A 3444 (from G17; see also Venturi et al. 2008, Kale et al. 2015). Panels *b* and *c* show radio/X-ray overlays for MACS J0429.6-0253 and MS 0839.8+2938, both cool cores in our supplementary sample. All three radio images have similar angular resolution ($\sim 5''$) and sensitivity ($1\sigma \sim 35 - 40$ μJy beam^{-1}). The observations also have similar sampling of short spacings in the *uv*–plane, that ensures the possibility of detecting

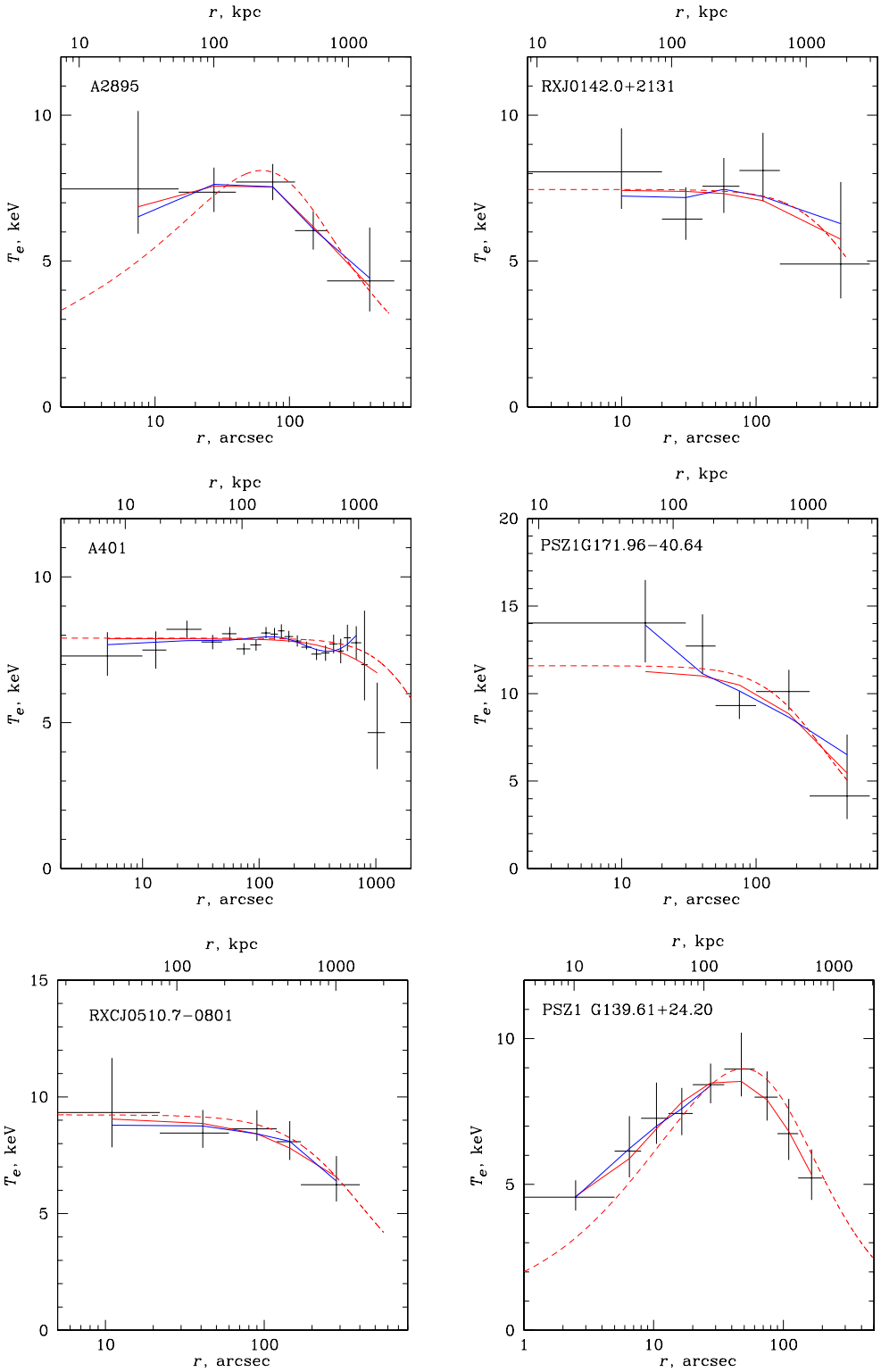

Figure 2. Temperature profiles for A 2895, RXC J0142.0+2131, A 401, PSZ1G171.96-40.64, RXC J0510.7-0801 and PSZ1G139.61+24.20. Crosses are the observed projected temperatures. Solid and dashed red lines show the best-fit three-dimensional model and the corresponding projected profile, respectively, and solid blue lines show the best-fit entropy model (§5.5 and Table 5).

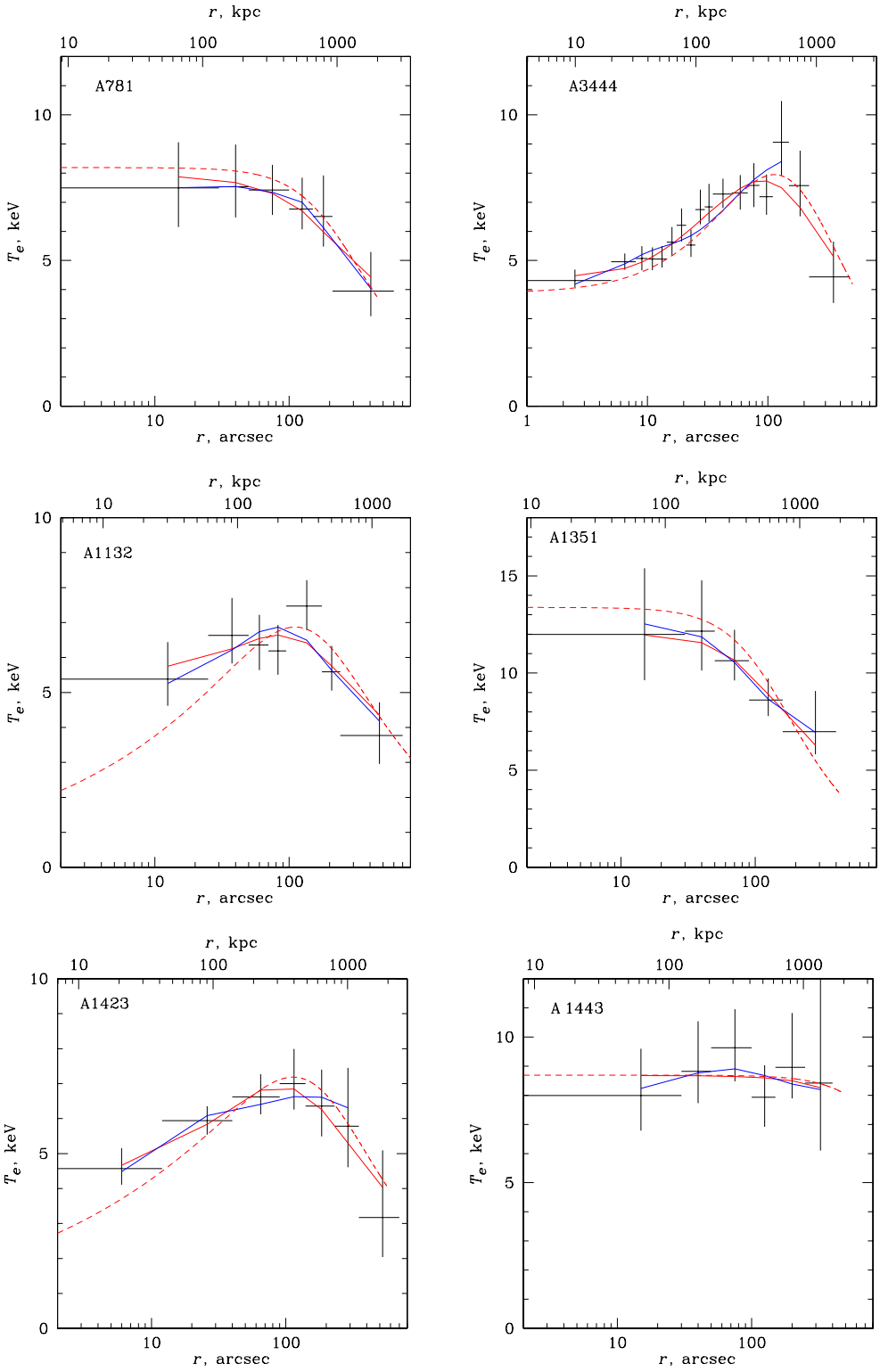

Figure 3. Same as Fig. 2, but for A 781, A 3444, A 1132, A 1351, A 1423 and A 1443.

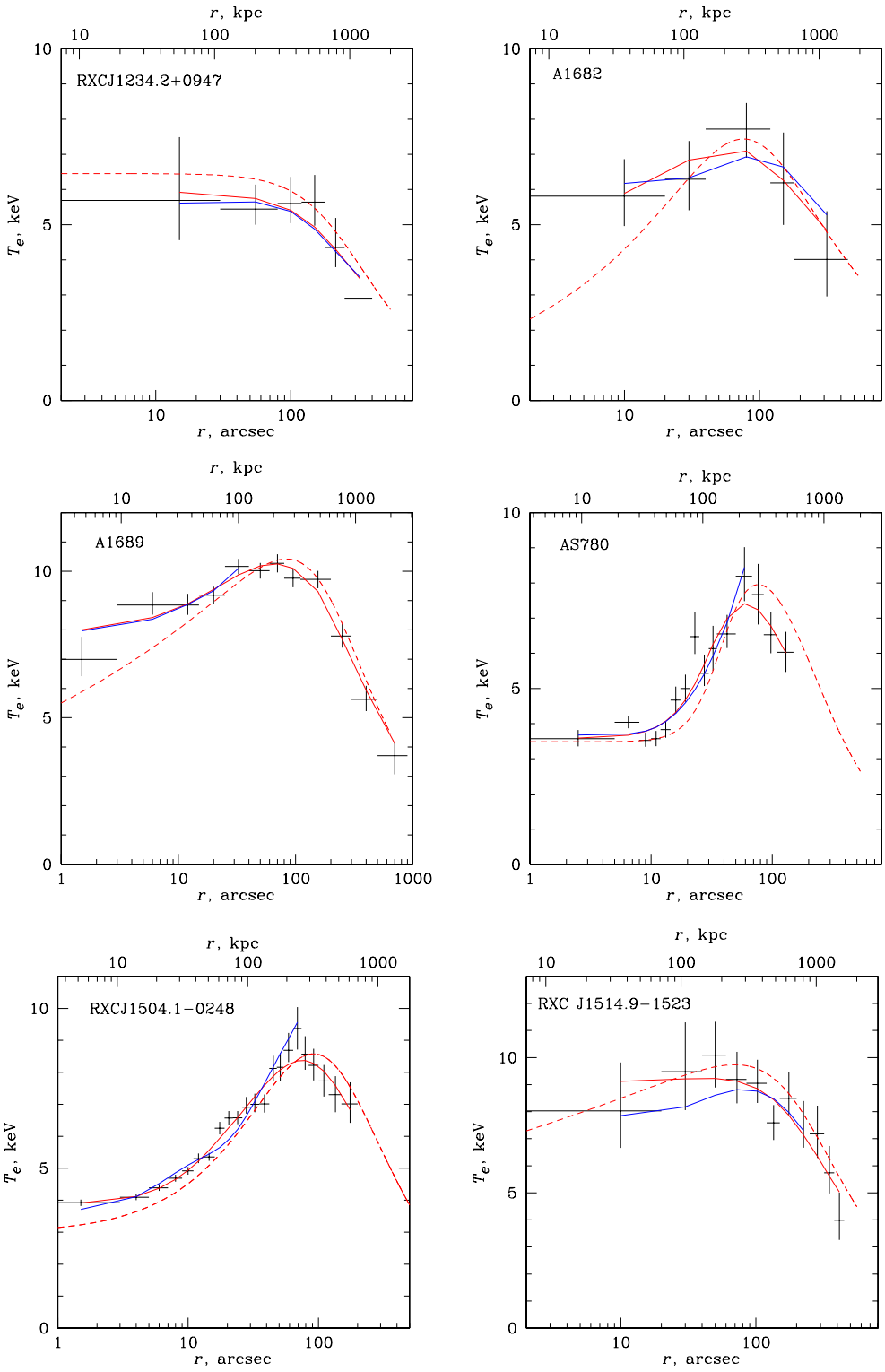

Figure 4. Same as Fig. 2, but for RXC J1234.2+0947, A 1682, A 1689, AS 780, RXC J1504.1-0248 and RXC J1514.9-1523.

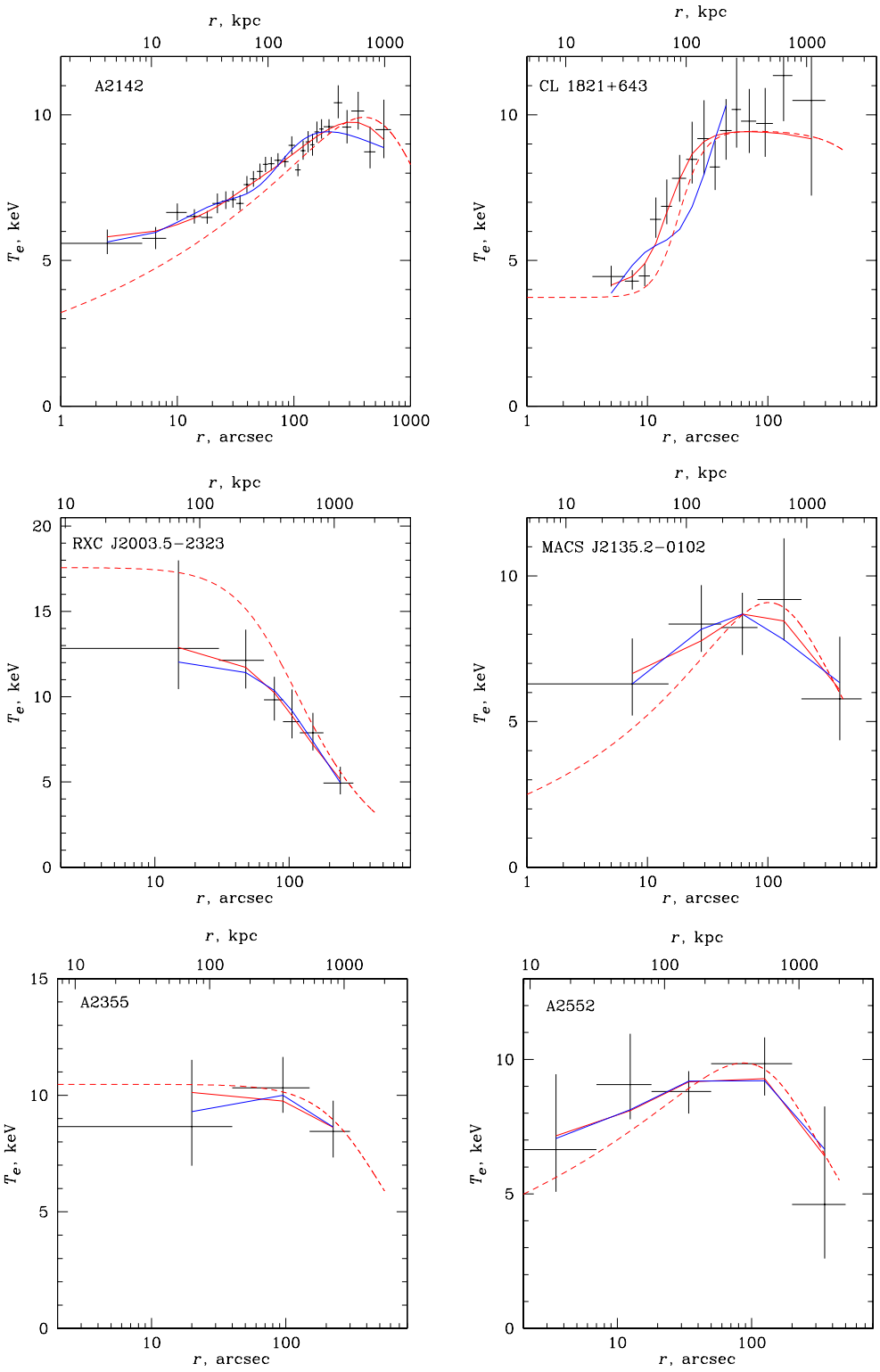

Figure 5. Same as Fig. 2, but for A 2142, CL 1821+643, RXC J2003.5-2323, MACS J2135.2-0102, A 2355 and A 2552.

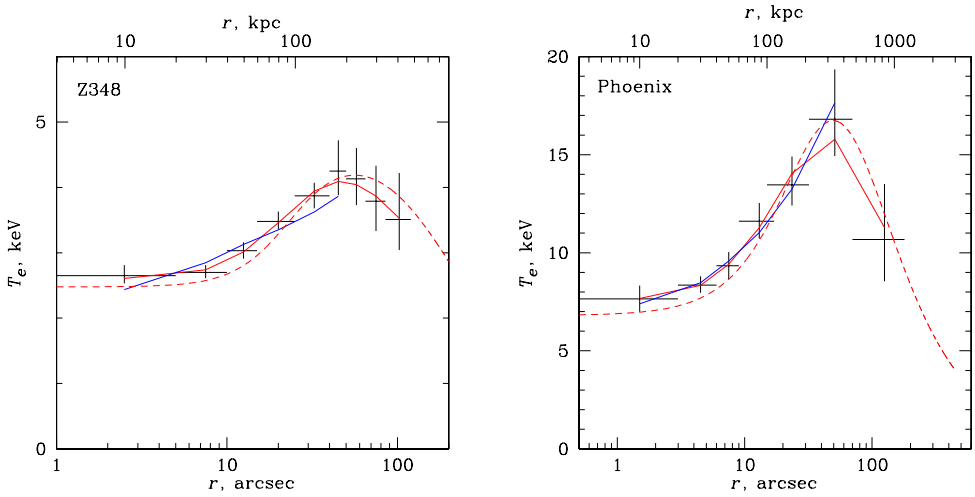

Figure 6. Same as Fig. 2, but for Z348 and the Phoenix cluster.

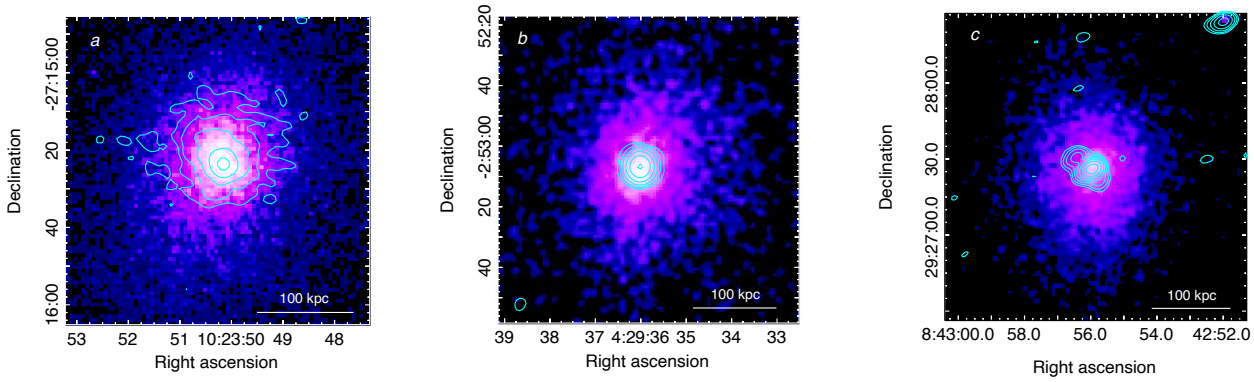

Figure 7. *(a):* Radio minihalo in the cool core of A 3444, overlaid on the *Chandra* 0.5-4 keV image. The radio contours are from a *VLA* BnA–configuration image at 1.4 GHz (from G17). The restoring beam is 5″ and *rms* noise is 35 μJy beam^{-1}. Contours are 0.09, 0.18, 0.36, 0.72, 1.44 mJy beam^{-1}. *(b,c):* examples of two cool-core clusters, MACS J0429.6-0253 and MS 0839.8+2938, without a minihalo. For both clusters, the *VLA* B–configuration images at 1.4 GHz are overlaid as contours on the *Chandra* 0.5-4 keV image. For MACS J0429.6-0253, the restoring beam is 5″ × 4″ and *rms* noise is 40 μJy beam^{-1}. Contours are 0.1, 0.4, 1.6, 6.4, 25.6, 104.4 mJy beam^{-1}. For MS 0839.8+2938, the restoring beam is 6″ × 4″ and *rms* noise is 40 μJy beam^{-1}. Contours start at $+3\sigma$ and then scale by a factor of 2.

extended emission on a largest scale of $\sim 2'$. This corresponds to a physical scale of $\sim$ 470 kpc for A 3444, $\sim$ 640 kpc for MACS J0429.6-0253 and $\sim$ 390 kpc for MS 0839.8+2938, thus well beyond the region occupied by the central radio galaxy. While a minihalo is clearly well detected in A 3444, no indication of diffuse radio emission is visible in the cores of the other clusters at a similar sensitivity level.

7. DISCUSSION

The purpose of this study is to quantify how frequent are radio minihalos in clusters. Top panels in Fig. 8 plot the clusters in our mass-limited sample in the $M_{500} - K_0$ and $T_{\rm X,\,ce} - K_0$ planes (in the latter panel, the approximate temperature from the $M_{500} - T_{\rm X}$ relation that corresponds to our mass cut is shown by a dashed line). As noted by C09, Rossetti et al. (2013) and others, the cluster sample clearly separates into two populations, cool cores with $K_0 \lesssim 30$ keV cm^2 and non-cool cores (most of which obvious mergers) with $K_0 \gtrsim 50$ keV cm^2. The fraction of cool cores in our *Planck*-selected sample is 26% (15 out of 58), similar to the fraction found in a much larger *Planck*-selected sample (Andrade-Santos et

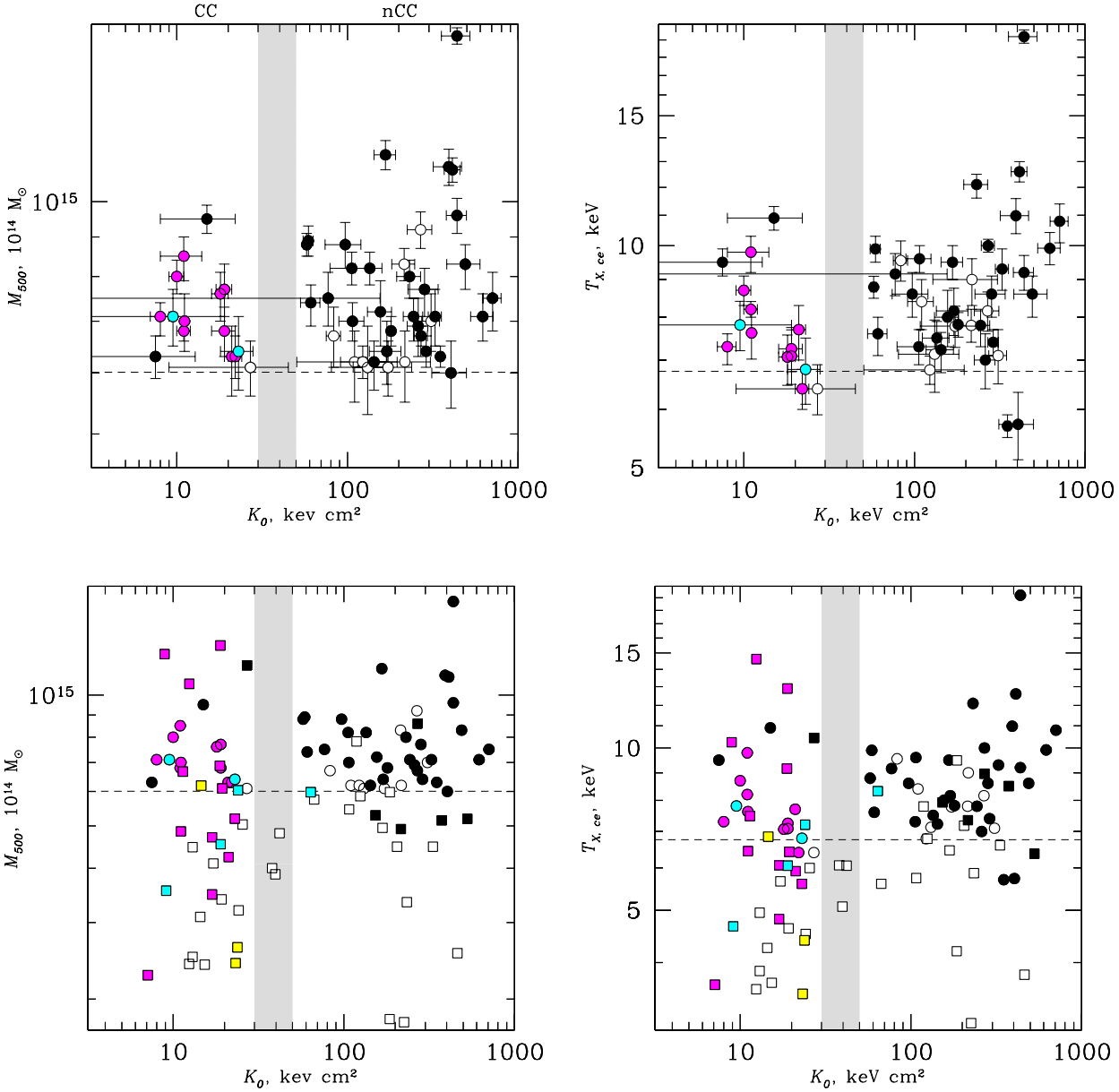

Figure 8. *Upper panels*: $M_{500} - K_0$ and $T_{\mathrm{X,ce}} - K_0$ plots for the *Chandra* clusters in our statistical sample. Clusters with minihalos are shown as magenta (confirmed detections) and cyan (candidates), radio-halo clusters (including candidates) are shown in black and empty circles are clusters with no detected central diffuse radio emission. Clusters without high-sensitivity radio observations (RXC J0510.7-0801, RXC J0520.7-1328, MACS J2135.2-0102, A 2355 and A 1733) are not included in the plots (they all have $K_0 > 80$ kev cm^2; Table 6.) *Lower panels*: Same for the combined statistical sample (circles) and supplementary sample (squares). Error bars are omitted for clarity. Symbol colors are the same. Yellow shows clusters hosting a central diffuse radio source whose classification as a minihalo is uncertain (ZwCl 1742.1+3306, MACS J1931.8–2634, A2626; §3.2). The combined sample extends to lower masses, where minihalos appear to be less frequent.

Table 6. Temperatures and core entropies for statistical sample

Cluster name	$T_{\rm X,\,ce}$ (keV)	K_0 (keV cm^2)	Ref.	Cluster name	$T_{\rm X,\,ce}$ (keV)	K_0 (keV cm^2)	Ref.
A 2744	$9.2^{+0.7}_{-0.6}$	438 ± 59	2, 3	RXC J1234.2+0947	$5.7^{+0.4}_{-0.4}$	404 ± 93	1, 1
A 68	$9.0^{+1.5}_{-1.1}$	217 ± 89	2, 3	A 1682	$7.2^{+0.6}_{-0.5}$	143 ± 26	1, 1
A 2813	$8.2^{+0.5}_{-0.5}$	268 ± 44	1, 3	A 1689	$9.9^{+0.2}_{-0.2}$	59 ± 4	1,1
A 2895	$7.8^{+0.5}_{-0.5}$	173 ± 65	1, 1	A 1733	$9.1^{+1.8}_{-1.3}$	332 ± 148[a]	1, 1
A 209	$7.3^{+0.6}_{-0.5}$	106 ± 27	2, 3	A 1758a	$12.1^{+1.2}_{-0.9}$	231 ± 37	2, 3
RXC J0142.0+2131	$7.1^{+0.6}_{-0.5}$	131 ± 51	1, 1	A 1763	$7.8^{+0.7}_{-0.6}$	215 ± 33	2, 3
MACS J0257.6−2209	$8.0^{+1.1}_{-0.9}$	156 ± 25	2, 3	A 1835 (MH)	$9.8^{+0.6}_{-0.5}$	11 ± 3	2, 3
A 401	$7.8^{+0.6}_{-0.6}$	180 ± 6	1, 1	A 1914	$9.6^{+0.6}_{-0.5}$	107 ± 18	2, 3
A 3088	$9.6^{+0.7}_{-0.7}$	83 ± 8	1, 3	AS 780 (MH)	$7.1^{+0.3}_{-0.3}$	19 ± 2	1, 1
PSZ1G171.96−40.64	$11.0^{+0.9}_{-0.5}$	329 ± 74	1, 1	RXC J1504.1−0248 (MH)	$7.6^{+0.1}_{-0.1}$	11.1 ± 0.3	1, 1
A 478 (MH)	$7.3^{+0.3}_{-0.2}$	8 ± 1	2, 3	A 2029 (MH)	$8.2^{+0.3}_{-0.3}\star$	11 ± 1	2, 3
A 521	$7.0^{+0.6}_{-0.5}$	260 ± 36	2, 3	RXC J1514.9−1523	$8.6^{+0.4}_{-0.3}$	490 ± 108	1, 1
A 520	$9.3^{+0.7}_{-0.6}$	326 ± 29	2, 3	A 2142	$8.8^{+0.1}_{-0.1}$	58 ± 2	1, 1
RXC J0510.7−0801	$8.4^{+0.5}_{-0.4}$	158 ± 99	1, 1	A 2163	$19.2^{+0.9}_{-0.8}$	438 ± 83	2, 3
RXCJ 0520.7−1328	$6.4^{+0.8}_{-0.7}$	89 ± 22	2, 3	A 2204 (MH)	$8.7^{+0.6}_{-0.5}$	10 ± 1	2, 3
PSZ1G139.61+24.20 (cMH)	$7.5^{+0.4}_{-0.4}$	10 ± 10	1, 1	A 2218	$7.3^{+0.4}_{-0.4}$	289 ± 20	2, 3
A 665	$7.5^{+0.4}_{-0.3}$	135 ± 24	2, 3	A 2219	$12.6^{+0.7}_{-0.6}\star$	412 ± 43	2, 3
A 697	$9.5^{+0.9}_{-0.8}$	167 ± 24	2, 3	A 2256	$5.7^{+0.2}_{-0.2}\star$	350 ± 12	2, 3
A 754	$10.0^{+0.3}_{-0.3}$	270 ± 24	4, 3	RXC J1720.1+2637 (MH)	$6.4^{+0.3}_{-0.3}$	21 ± 2	2, 3
A 773	$7.8^{+0.7}_{-0.6}$	244 ± 32	2, 3	A 2261	$7.6^{+0.5}_{-0.4}$	61 ± 8	2, 3
A 781	$8.2^{+0.7}_{-0.6}$	170 ± 36	1, 1	CL 1821+643	$9.5^{+0.4}_{-0.4}$	8 ± 5	1, 1
RBS 797 (MH)	$7.7^{+0.9}_{-0.8}$	21 ± 2	2, 3	RXC J2003.5−2323	$10.8^{+0.8}_{-0.6}$	708 ± 85	1, 1
A 3444 (MH)	$7.1^{+0.2}_{-0.2}$	18 ± 2	1, 1	MACS J2135.2−0102	$8.6^{+0.8}_{-0.6}$	142 ± 18	1, 1
A 1132	$6.8^{+0.6}_{-0.5}$	154 ± 31	1, 1	A 2355	$9.4^{+0.9}_{-0.9}$	519 ± 117	1, 1
RXC J1115.8+0129 (cMH)	$6.8^{+1.2}_{-0.9}$	23 ± 5	2, 3	A 2390	$10.9^{+0.3}_{-0.3}$	15 ± 7	2, 3
A 1300	$8.6^{+1.2}_{-1.0}$	97 ± 23	2, 3	A 2537	$8.4^{+0.8}_{-0.7}$	110 ± 19	2, 3
A 1351	$9.9^{+0.7}_{-0.7}$	620 ± 93	1, 1	A 2552	$9.2^{+0.7}_{-0.7}$	78 ± 33	1, 1
A 1423	$6.4^{+0.3}_{-0.3}$	27 ± 18	1, 1	A 2631	$7.1^{+1.1}_{-0.8}$	309 ± 37	2, 3
A 1443	$8.6^{+0.6}_{-0.4}$	283 ± 57	1, 1	A 2667 (MH)	$7.3^{+0.4}_{-0.4}$	19 ± 3	1, 3

[a] from the temperature measured within the central $r = 120$ kpc.

NOTE—Column 1: cluster name. The presence of a minihalo or a candidate is indicated as MH and cMH, respectively. Column 2: temperature within R_{2500} (R_{5000} for those clusters marked with $\star$) measured in the $0.7 - 7$ keV band; the central $r = 70$ kpc region has been excised for all clusters except A 754. Column 3: core entropy. Column 4: references for temperature and the core entropy floor, respectively: (1) this work, (2) C08, (3) C09, (4) Markevitch et al. (2003).

Table 7. Temperatures and core entropies for supplementary sample

Cluster name	$T_{\rm X,\,ce}$ (keV)	K_0 (keV cm^2)	Ref.	Cluster name	$T_{\rm X,\,ce}$ (keV)	K_0 (keV cm^2)	Ref.
Z348	$3.9^{+0.1}_{-0.1}$	13 ± 1	1,1	A 1413 (cMH)	$8.3^{+0.2}_{-0.2}$	64 ± 8	1,3
A 119	$5.9^{+0.3}_{-0.3}\star$	234 ± 88	2,3	A 1576	$9.5^{+0.7}_{-0.7}$	186 ± 49	1,3
A 141	$7.2^{+0.6}_{-0.5}$	205 ± 27	1,3	A 1650	$6.1^{+0.1}_{-0.1}$	38 ± 10	1,3
A 193	$4.2^{+1.0}_{-0.6}$	186 ± 13	5,3	RX J1347.5−1145 (MH)	$14.6^{+1.0}_{-0.8}$	13 ± 21	2,3
A 267	$6.7^{+0.6}_{-0.5}$	169 ± 18	2,3	A 1795 (cMH)	$6.1^{+0.2}_{-0.2}\star$	19 ± 1	2,3
MACS J0159.8−0849 (MH)	$9.2^{+0.7}_{-0.6}$	19 ± 4	2,3	A 1995	$8.4^{+0.7}_{-0.6}$	374 ± 60	2,3
A 383	$4.9^{+0.3}_{-0.3}$	13 ± 2	2,3	MS 1455.0+2232 (MH)	$4.8^{+0.1}_{-0.1}$	17 ± 2	2,3
A 399	$8.0^{+0.4}_{-0.3}$	153 ± 19	2,3	A 2034	$7.2^{+0.2}_{-0.2}$	233 ± 23	2,3
Perseus (MH)	$6.4^{+0.1}_{-0.1}$	19.4 ± 0.2	4,3	RX J1532.9+3021 (MH)	$6.0^{+0.4}_{-0.4}$	17 ± 2	2,3
MACS J0329.6−0211 (MH)	$6.3^{+0.5}_{-0.4}$	11 ± 3	2,3	A 2111	$7.1^{+1.3}_{-1.0}$	107 ± 97	2,3
2A 0335+096 (MH)	$3.6^{+0.1}_{-0.1}$	7.1 ± 0.1	5,3	A 2125	$2.9^{+0.3}_{-0.3}$	225 ± 32	2,3
MACS J0417.5−1154	$11.1^{+2.0}_{-1.5}$	27 ± 7.3	2,3	Ophiuchus (MH)	$10.3^{+0.2}_{-0.2}$	9 ± 1	4,3
MACS J0429.6−0253	$5.7^{+0.6}_{-0.5}$	17 ± 4.3	2,3	A 2255	$6.1^{0.2}_{-0.2}$	529 ± 28	2,3
RX J0439.0+0715	$5.6^{+0.4}_{-0.3}$	67 ± 19	2,3	RX J1720.2+3536 (cMH)	$7.2^{+0.5}_{-0.5}$	24 ± 3	2,3
MS 0440.5+0204	$6.0^{+0.9}_{-0.7}\star$	26 ± 8	2,3	ZwCl 1742.1+3306 (u)	$4.4^{+0.2}_{-0.2}$	24 ± 2	1,3
A 611	$7.1^{+0.6}_{-0.5}$	125 ± 19	2,3	A 2319	$8.8^{+0.3}_{-0.2}$	270 ± 5	4,3
MS 0839.8+2938	$4.7^{+0.3}_{-0.3}$	19 ± 3	2,3	MACS J1931.8−2634 (u)	$7.0^{+0.7}_{-0.6}$	15 ± 4	2,3
Z2089	$4.4^{+0.2}_{-0.2}$	24 ± 5	1,3	RX J2129.6+0005 (MH)	$7.3^{+0.3}_{-0.3}$	21 ± 4	1,3
ZwCl 2701	$5.2^{+0.3}_{-0.3}$	40 ± 4	2,3	A 2420	$6.6^{+0.2}_{-0.2}$	333 ± 68	1,3
A 907 (MH)	$5.6^{+0.2}_{-0.2}$	23 ± 3	2,3	MACS J2228.5+2036	$7.9^{+1.1}_{-0.9}$	119 ± 39	2,3
ZWCL 3146 (MH)	$7.5^{+0.3}_{-0.3}$	11 ± 2	2,3	MACS J2245.0+2637	$6.1^{+0.6}_{-0.5}$	42 ± 7	2,3
A 1068 (cMH)	$4.7^{+0.2}_{-0.2}\star$	9 ± 1	2,3	A 2556	$3.6^{+0.2}_{-0.2}\star$	12 ± 1	2,3
A 1204	$3.6^{+0.2}_{-0.2}$	15 ± 1	2,3	A 2626 (u)	$3.6^{+0.1}_{-0.1}$	23 ± 3	1,3
A 1240	$4.4^{+0.3}_{-0.3}$	462 ± 42	1,3	Phoenix (MH)	$12.9^{+0.7}_{-0.7}$	19 ± 3	1,1

NOTE—Column 1: cluster name. The presence of a minihalo, a candidate minihalo or a central diffuse source with uncertain classification (§3.2) are indicated as MH, cMH and u respectively. Column 2: cluster global temperature within R_{2500} (R_{5000} for those clusters marked with $\star$) measured in the $0.7 - 7$ keV band; the central $r = 70$ kpc region has been excised for all clusters except Perseus, 2A 0335+096, Ophiuchus, A 193 and A 2319. Column 3: core entropy. Column 4: references for temperature and the core entropy floor: (1) this work, (2) C08, (3) C09, (4) Ikebe et al. (2002), (5) David et al. (1993).

al. 2017) and lower than that seen in X-ray selected samples of nearby clusters (e.g., Rossetti et al. 2016).

As shown before (e.g., Cassano et al. 2013, Rossetti et al. 2013, Cuciti et al. 2015, Yuan et al. 2015), giant halos (black symbols) are found almost exclusively in non-cool core clusters. We find that minihalos (magenta symbols) are indeed found exclusively in cool cores, confirming previous non-statistical findings (e.g., Giacintucci et al. 2014a, Yuan et al. 2015, Kale et al. 2015). A new result that is evident in Fig. 8 (top panels) is that *almost all* cool cores in a complete sample of massive clusters — 12 out of 15, or 80% — possess a minihalo. Radio minihalos are not that rare after all.

It is interesting to extend the mass range of the sample toward lower masses and temperatures. According to Cuciti et al. (2015), the probability of finding a giant radio halo in merging clusters increases with the total mass. This is instructive for the origin of giant halos, because it implies a statistical link between the mechanical energy available during mergers and the generation of these sources (e.g., Cassano et al. 2006, 2016). It is interesting to check if minihalos exhibit a similar behavior. Lower panels in Fig. 8 show our combined statistical + supplementary sample, which includes all the known 22 confirmed minihalos (magenta points) and 6 candidates (cyan points). This combined sample extends a factor 3 below the mass cut of the statistical one, as well as adding a number of massive systems. We do see the lower frequency of the giant radio halos in cooler clusters, observed in Cassano et al. (2013) and Cuciti et al. (2015). Similarly, at lower masses, a large fraction of cool cores without minihalos (not detected at a similar radio sensitivity; see §5, Fig. 7 and Appendix A) emerges, while almost all the additional *massive* cool

cores do have minihalos, consistently with our finding for the statistical sample. Minihalos are still absent in the non-cool-core clusters (with the exception of the candidate minihalo in A 1413); a few "warm cores" that appear in the $K_0 = 30 - 50$ keV cm^2 gap do not host minihalos (or giant halos) either. The apparent reduced frequency of minihalos at lower masses needs a proper statistical investigation that accounts for selection effects (e.g., what if the radio luminosity correlates with the cluster mass) and radio upper limits (for instance via injection of *fake* minihalos in the *uv*–data, e.g., Kale et al. 2015), which will be the subject of future work.

8. CONCLUSIONS

The two new results of our study are: (a) almost all (12 out of 15, i.e., 80%) massive clusters with cool cores ($M_{500} > 6 \times 10^{14} M_\odot$ or $T \gtrsim 6$ keV) exhibit a radio minihalo, and (b) the fraction of minihalos appears to drop in cool cores with lower cluster total masses (or global temperatures). To make the former observation, we used a mass-limited cluster sample. For the latter result, we extended the sample to include more clusters with available *Chandra* and radio data, including higher-redshift and lower-mass clusters and all the other known minihalos (for a total of 28 minihalos, including 6 candidates).

These findings may encode information on the origin of minihalos. In the present study, we used only the presence or absence of a minihalo; we will investigate the correlation of the radio power with cluster mass, as well as with cool core thermodynamic parameters, in the follow-up works. A few outliers may prove especially valuable, such as a minihalo in a low-mass cool core 2A 0335+096 (Sarazin et al. 1995), a giant halo in a high-mass cool core CL 1821+643 (Bonafede et al. 2014; Kale & Parekh 2016), a halo in A 2390 (Sommer et al. 2017) whose cool core has a similar, unusually large radius (Vikhlinin et al. 2005), as well as the absence of minihalos in warm cores.

Acknowledgements.
We thank the referee for their critical and helpful comments. SG acknowledges the support by the National Aeronautics and Space Administration, through *Chandra* Award Numbers G03-14140X, AR5-16013X and G05-16136X. Basic research in radio astronomy at the Naval Research Laboratory is supported by 6.1 Base funding. RC, TV and GB acknowledge partial support from PRIN INAF 2014. This research has made use of the NASA/IPAC Extragalactic Database (NED) which is operated by the Jet Propulsion Laboratory, California Institute of Technology, under contract with the National Aeronautics and Space Administration. The National Radio Astronomy Observatory is a facility of the National Science Foundation operated under cooperative agreement by Associated Universities, Inc.

REFERENCES

Andrade-Santos, F., Jones, C., Forman, W., et al., 2017, ApJ, submitted, arXiv:1703.08690

Ascasibar, Y., & Markevitch, M. 2006, ApJ, 650, 102

Bacchi, M., Feretti, L., Giovannini, G., & Govoni, F. 2003, A&A, 400, 465

Barrena, R., Boschin, W., Girardi, M., & Spolaor, M. 2007, A&A, 469, 861

Bonafede, A., Giovannini, G., Feretti, L., Govoni, F., & Murgia, M. 2009, A&A, 494, 429

Bonafede, A., Intema, H. T., Brüggen, M., et al. 2014, MNRAS, 444, L44

Bonafede, A., Intema, H., Brüggen, M., et al. 2015, MNRAS, 454, 3391

Briggs, D. S. 1995, Bulletin of the American Astronomical Society, 27, 112.02

Bravi, L., Gitti, M., & Brunetti, G. 2016, MNRAS, 455, L41

Brentjens, M. A. 2008, A&A, 489, 69

Brunetti, G., Giacintucci, S., Cassano, R., et al. 2008, Nature, 455, 944

Brunetti, G., & Jones, T. W. 2014, International Journal of Modern Physics D, 23, 1430007

Burns, J. O., Sulkanen, M. E., Gisler, G. R., & Perley, R. A. 1992, ApJL, 388, L49

Cassano, R., & Brunetti, G. 2005, MNRAS, 357, 1313

Cassano, R., Brunetti, G., & Setti, G. 2006, MNRAS, 369, 1577

Cassano, R., Brunetti, G., Setti, G., Govoni, F., & Dolag, K. 2007, MNRAS, 378, 1565

Cassano, R., Gitti, M., & Brunetti, G. 2008, A&A, 486, L31

Cassano, R., Ettori, S., Giacintucci, S., et al. 2010, ApJL, 721, L82

Cassano, R., Ettori, S., Brunetti, G., et al. 2013, ApJ, 777, 141

Cassano, R., Brunetti, G., Giocoli, C., & Ettori, S. 2016, A&A, 593, A81

Cavagnolo, K. W., Donahue, M., Voit, G. M., & Sun, M. 2008, ApJ, 682, 821 (C08)

Cavagnolo, K. W., Donahue, M., Voit, G. M., & Sun, M. 2009, ApJS, 182, 12 (C09)
Cavaliere, A., & Fusco-Femiano, R. 1978, A&A, 70, 677
Clarke, T. E., & Ensslin, T. A. 2006, AJ, 131, 2900
Crawford, C. S., Allen, S. W., Ebeling, H., Edge, A. C., & Fabian, A. C. 1999, MNRAS, 306, 857
Cuciti, V., Cassano, R., Brunetti, G., et al. 2015, A&A, 580, A97
Dallacasa, D., Brunetti, G., Giacintucci, S., et al. 2009, ApJ, 699, 1288
David, L. P., Slyz, A., Jones, C., et al. 1993, ApJ, 412, 479
Doria, A., Gitti, M., Ettori, S., et al. 2012, ApJ, 753, 47
Ehlert, S., Allen, S. W., von der Linden, A., et al. 2011, MNRAS, 411, 1641
Farnsworth, D., Rudnick, L., Brown, S., & Brunetti, G. 2013, ApJ, 779, 189
Feretti, L., Boehringer, H., Giovannini, G., & Neumann, D. 1997, A&A, 317, 432
Feretti, L., Giovannini, G., Boehringer, H. 1997, New Astronomy, 2, 501
Feretti, L., Fusco-Femiano, R., Giovannini, G., & Govoni, F. 2001, A&A, 373, 106
Feretti, L., Schuecker, P., Böhringer, H., Govoni, F., & Giovannini, G. 2005, A&A, 444, 157
Feretti, L., Giovannini, G., Govoni, F., & Murgia, M. 2012, A&A Rv, 20, 54
Ferrari, C., Intema, H. T., Orrù, E., et al. 2011, A&A, 534, L12
Fujita, Y., Kohri, K., Yamazaki, R., & Kino, M. 2007, ApJL, 663, L61
Fujita, Y., & Ohira, Y. 2011, ApJ, 738, 182
Fujita, Y., & Ohira, Y. 2013, MNRAS, 428, 599
Gendron-Marsolais, M., Hlavacek-Larrondo, J., van Weeren, R. J., et al. 2017, arXiv:1701.03791
Giacintucci, S., Venturi, T., Cassano, R., Dallacasa, D., & Brunetti, G. 2009, ApJL, 704, L54
Giacintucci, S., Venturi, T., Brunetti, G., et al. 2009, A&A, 505, 45
Giacintucci, S., Markevitch, M., Brunetti, G., Cassano, R., & Venturi, T. 2011, A&A, 525, L10
Giacintucci, S., Dallacasa, D., Venturi, T., et al. 2011, A&A, 534, A57
Giacintucci, S., O'Sullivan, E., Clarke, T. E., et al. 2012, ApJ, 755, 172
Giacintucci, S., Kale, R., Wik, D. R., Venturi, T., & Markevitch, M. 2013, ApJ, 770, 161
Giacintucci, S., Markevitch, M., Venturi, T., et al. 2014a, ApJ, 781, 9
Giacintucci, S., Markevitch, M., Brunetti, G., et al. 2014b, ApJ, 795, 73
Giacintucci, S., et al., 2017, in preparation (G17)
Gioia, I. M., Shaya, E. J., Le Fèvre, O., et al. 1998, ApJ, 497, 573
Giovannini, G., & Feretti, L. 2000, New A, 5, 335
Giovannini, G., Bonafede, A., Feretti, L., et al. 2009, A&A, 507, 1257
Gitti, M., Tozzi, P., Brunetti, G., et al. 2015, Advancing Astrophysics with the Square Kilometre Array (AASKA14), 76
Gitti, M. 2013, MNRAS, 436, L84
Gitti, M., Brunetti, G., & Setti, G. 2002, A&A, 386, 456
Gitti, M., Brunetti, G., Feretti, L., & Setti, G. 2004, A&A, 417, 1
Gitti, M., Feretti, L., & Schindler, S. 2006, A&A, 448, 853
Gitti, M., Ferrari, C., Domainko, W., Feretti, L., & Schindler, S. 2007, A&A, 470, L25
Govoni, F., Feretti, L., Giovannini, G., et al. 2001, A&A, 376, 803
Govoni, F., Murgia, M., Feretti, L., et al. 2005, A&A, 430, L5
Govoni, F., Murgia, M., Markevitch, M., et al. 2009, A&A, 499, 371
Govoni, F., Murgia, M., Giovannini, G., Vacca, V., & Bonafede, A. 2011, A&A, 529, A69
Guo, F., & Oh, S. P. 2008, MNRAS, 384, 251
Hitomi Collaboration, Aharonian, F., Akamatsu, H., et al. 2016, Nature, 535, 117
Hlavacek-Larrondo, J., Allen, S. W., Taylor, G. B., et al. 2013, ApJ, 777, 163
Hogan, M. T., Edge, A. C., Hlavacek-Larrondo, J., et al. 2015, MNRAS, 453, 1201
Ikebe, Y., Reiprich, T. H., Böhringer, H., Tanaka, Y., & Kitayama, T. 2002, A&A, 383, 773
Jacob, S., & Pfrommer, C. 2017a, MNRAS, arXiv:1609.06321
Jacob, S., & Pfrommer, C. 2017b, MNRAS, arXiv:1609.06322
Jones, C., & Forman, W. 1984, ApJ, 276, 38
Kalberla, P. M. W., Burton, W. B., Hartmann, D., et al. 2005, A&A, 440, 775
Kale, R., Venturi, T., Giacintucci, S., et al. 2013, A&A, 557, A99
Kale, R., Venturi, T., Giacintucci, S., et al. 2015, A&A, 579, A92
Kale, R., & Parekh, V. 2016, MNRAS, 459, 2940
Kassim, N. E., Clarke, T. E., Enßlin, T. A., Cohen, A. S., & Neumann, D. M. 2001, ApJ, 559, 785
Macario, G., Venturi, T., Brunetti, G., et al. 2010, A&A, 517, A43

Macario, G., Markevitch, M., Giacintucci, S., et al. 2011, ApJ, 728, 82
Macario, G., Venturi, T., Intema, H. T., et al. 2013, A&A, 551, A141
Macario, G., Intema, H. T., Ferrari, C., et al. 2014, A&A, 565, A13
Markevitch, M., Ponman, T. J., Nulsen, P. E. J., et al. 2000, ApJ, 541, 542
Markevitch, M., Mazzotta, P., Vikhlinin, A., et al. 2003, ApJL, 586, L19
Mazzotta, P., Rasia, E., Moscardini, L., & Tormen, G. 2004, MNRAS, 354, 10
Mazzotta, P., & Giacintucci, S. 2008, ApJL, 675, L9
McDonald, M., McNamara, B. R., van Weeren, R. J., et al. 2015, ApJ, 811, 111
McDonald, M., Allen, S. W., Bayliss, M., et al. 2017, arXiv:1702.05094
McNamara, B. R., & Nulsen, P. E. J. 2007, ARA&A, 45, 117
Mittal, R., Hudson, D. S., Reiprich, T. H., & Clarke, T. 2009, A&A, 501, 835
Murgia, M., Govoni, F., Markevitch, M., et al. 2009, A&A, 499, 679
Murgia, M., Govoni, F., Feretti, L., & Giovannini, G. 2010, A&A, 509, A86
Murgia, M., Eckert, D., Govoni, F., et al. 2010, A&A, 514, A76
Murgia, M., Parma, P., Mack, K.-H., et al. 2011, A&A, 526, A148
Murgia, M., Markevitch, M., Govoni, F., et al. 2012, A&A, 548, A75
Nagai, D. 2006, ApJ, 650, 538
Owen, F. N., Keel, W. C., Wang, Q. D., Ledlow, M. J., & Morrison, G. E. 2006, AJ, 131, 1974
Owen, F. N., Ledlow, M. J., Keel, W. C., Wang, Q. D., & Morrison, G. E. 2005, AJ, 129, 31
Owen, F. N., White, R. A., & Ge, J. 1993, ApJS, 87, 135
Owen, F. N., & Ledlow, M. J. 1997, ApJS, 108, 41
Pandey-Pommier, M., Richard, J., Combes, F., et al. 2016, arXiv:1612.00225
Parekh, V., van der Heyden, K., Ferrari, C., Angus, G., & Holwerda, B. 2015, A&A, 575, A127
Parekh, V., Dwarakanath, K. S., Kale, R., & Intema, H. 2017, MNRAS, 464, 2752
Perley, R. A., & Butler, B. J. 2013, ApJS, 204, 19
Pizzo, R. F., & de Bruyn, A. G. 2009, A&A, 507, 639
Planck Collaboration, Ade, P. A. R., Aghanim, N., et al. 2014, A&A, 571, 29
Pfrommer, C., & Enßlin, T. A. 2004, A&A, 413, 17
Pizzo, R. F., & de Bruyn, A. G. 2009, A&A, 507, 639
Reid, A. D., Hunstead, R. W., Lemonon, L., & Pierre, M. M. 1999, MNRAS, 302, 571
Rossetti, M., Eckert, D., De Grandi, S., et al. 2013, A&A, 556, A44
Rossetti, M., Gastaldello, F., Ferioli, G., et al. 2016, MNRAS, 457, 4515
Saikia, D. J., & Jamrozy, M. 2009, Bulletin of the Astronomical Society of India, 37, 63
Sarazin, C. L., Baum, S. A., & O'Dea, C. P. 1995, ApJ, 451, 125
Sijbring L.G., PhD Thesis, University of Groningen, A radio continuum and HI Line study of the Perseus cluster (1993)
Sommer, M. W., Basu, K., Intema, H., et al. 2017, MNRAS, 466, 996
Vacca, V., Govoni, F., Murgia, M., et al. 2011, A&A, 535, A82
Vacca, V., Feretti, L., Giovannini, G., et al. 2014, A&A, 561, A52
van Weeren, R. J., Röttgering, H. J. A., Brüggen, M., & Hoeft, M. 2010, Science, 330, 347
van Weeren, R. J., Intema, H. T., Lal, D. V., et al. 2014, ApJL, 786, L17
Venturi, T., Giacintucci, S., Brunetti, G., et al. 2007, A&A, 463, 937
Venturi, T., Giacintucci, S., Dallacasa, D., et al. 2008, A&A, 484, 327
Venturi, T., Giacintucci, G., Dallacasa, D., et al. 2011, MNRAS, 414, L65
Venturi, T., Giacintucci, S., & Dallacasa, D. 2011, Journal of Astrophysics and Astronomy, 32, 501
Venturi, T., Giacintucci, S., Dallacasa, D., et al. 2013, A&A, 551, A24
Venturi T., et al., 2017, A&A, in press (arXiv:1703.06802)
Vikhlinin, A., Markevitch, M., Murray, S. S., et al. 2005, ApJ, 628, 655
Vikhlinin, A., Kravtsov, A., Forman, W., et al. 2006, ApJ, 640, 691
Vikhlinin, A., Burenin, R. A., Ebeling, H., et al. 2009, ApJ, 692, 1033
White, D. A., Jones, C., & Forman, W. 1997, MNRAS, 292, 419
Yuan, Z. S., Han, J. L., & Wen, Z. L. 2015, ApJ, 813, 77
Zandanel, F., Pfrommer, C., & Prada, F. 2014, MNRAS, 438, 124
Zhuravleva, I., Churazov, E., Schekochihin, A. A., et al. 2014, Nature, 515, 85
ZuHone, J. A., Markevitch, M., Brunetti, G., & Giacintucci, S. 2013, ApJ, 762, 78

Table 8. Newly analyzed 1.4 GHz *VLA* observations

Cluster name	Configuration	Project	Date	Time (min)
A 193	C	AM735	2002 Nov 30	118
	C	AM702	2002 Oct 28	37
	D	AM702	2001 Oct 15	55
A 383	A	AR369	1996 Nov 17	54
	A	AR369	1996 Nov 19	100
	C	AM072	2002 Oct 28	61
	D	AM072	2001 Oct 21	60
MS 0440.5+0204	A	AI0072	1998 Apr 19,20	360
	C	AS0873	2006 Dec 14	43
MACS J0429.6-0253	A	AT0318	2006 Apr 03	52
	B	AT0318	2006 Sep 06	35
MS 0839.8+2938	B	AH0190	1985 Apr 25	30
	C	AH0491	1993 Jun 26	58
A 1204	C	AJ0242	1994 Dec 05	74
A 2125	C	AD0311	1993 Jul 29	343
A 2420	CnB	AM0702	2002 Sep 24,29	60
	DnC	AM0702	2001 Oct 6,7	60
A 2556	CnB	AM0702	2002 Sep 29	60
	DnC	AM0702	2001 Oct 07	60

NOTE—Column 1: cluster name. Column 2: *VLA* configuration. Columns 3 and 4: project code and observation date. Column 5: total time on source.

APPENDIX

A. RADIO OBSERVATIONS AND IMAGES

Table 8 lists the *VLA* archival observations at 1.4 GHz reanalyzed in this work, as described in §6. Our final radio images are presented and compared to the cluster optical images (from SDSS[7], POSS-2[8] or *HST* WFPC2[9]) and X-ray *Chandra* images in Figs. 9, 10 and Fig. 11. The radio images of MACS J0429.6-0253 and MS 0839.8+2938 are overlaid on the *Chandra* images in Fig. 7 and on the optical *HST* images in Fig. 10 (upper panels). The image properties are summarized in Table 9. All the images shown here have been obtained with the ROBUST parameter set to 0 in the AIPS task IMAGR. The flux density of the unresolved radio galaxies was measured by fitting the sources with a Gaussian model (task JMFIT). For extended radio galaxies, the total flux density was determined using the task TVSTAT. All fluxes were measured on images corrected for the primary-beam attenuation. A brief description of the radio emission in each individual cluster is given below.

A.1. *Notes on individual clusters*

A 193. The combined C and D–configuration image (Fig. 9, right upper panel) shows a central double radio source with a flux density of 61 ± 3 mJy. The combined C–configuration image (Fig. 9, left upper panel) reveals the source to be composed of a bright compact component, coincident with the cluster central galaxy, and a ~ 60 kpc-long "tail" toward North-East (see also Owen et al. (1993) and Owen & Ledlow (1997)). The total flux in this image is 60 ± 3 mJy, of which 28 ± 1 mJy are in the compact component.

[7] Sloan Digital Sky Survey.
[8] Second Palomar Observatory Sky Survey.
[9] *Hubble Space Telescope* Wide-Field Planetary Camera 2.

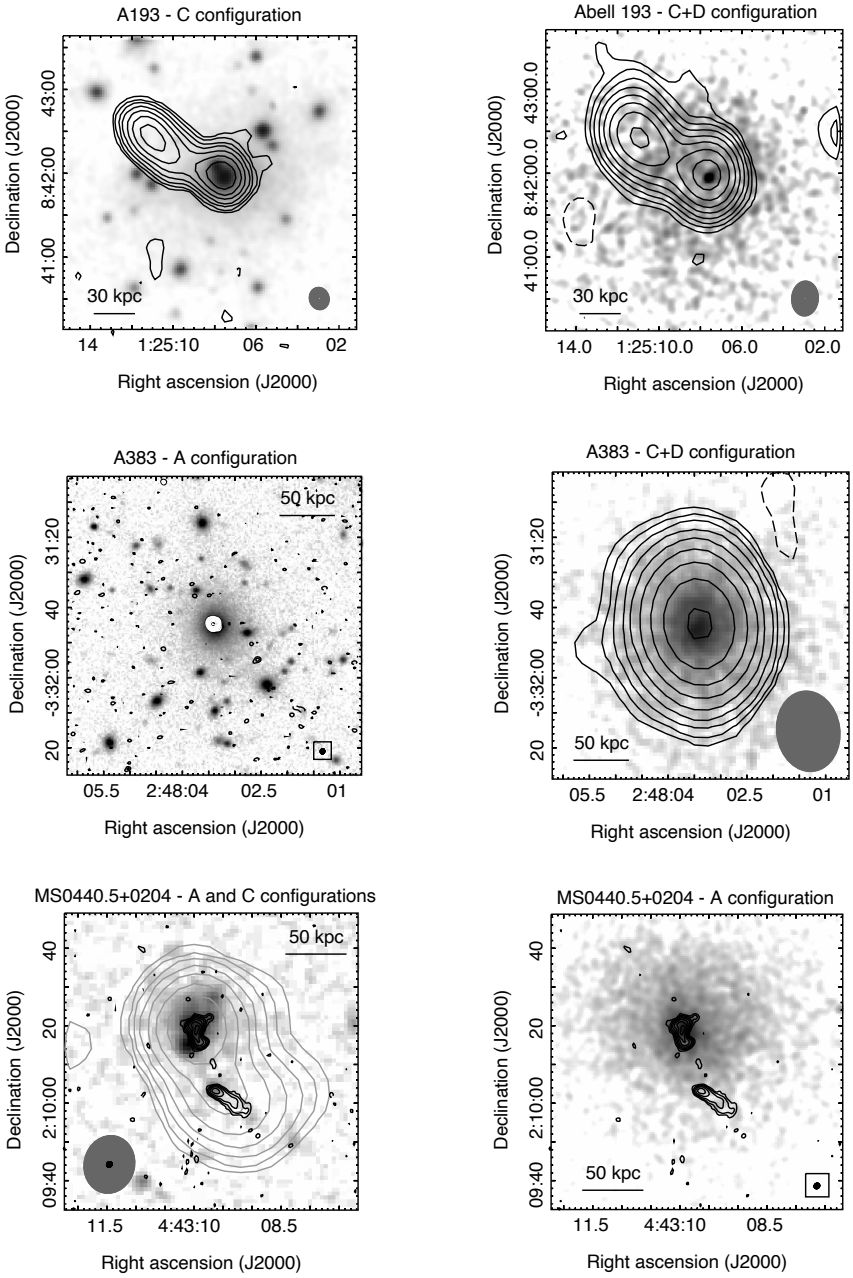

Figure 9. Upper and middle panels: *VLA* 1.4 GHz combined radio images of A 193 and A 383, overlaid on the optical r-band SDSS images (left) and smoothed X-ray *Chandra* images in the 0.5-4 keV band (right). Contours start at $+3\sigma$ and then scale by a factor of 2. When present, contours at -3σ are shown as dashed. Restoring beams (also shown as ellipses in the lower corner of each image) and *rms* noise values are as listed in Table 9. Bottom panels: *VLA* C–configuration (gray contours) and A–configuration (black contours) images of MS 0440.5+020, overlaid on the POSS–2 red optical image (left). On the right, the A–configuration image is overlaid on the smoothed X-ray *Chandra* image in the 0.5-4 keV band. Contours start from $+3\sigma$ and then scale by a factor of 2. No levels at -3σ are present in the portion of the images shown. Restoring beams (also shown as ellipses in the lower right corner of each image) and *rms* noise values are as listed in Table 9.

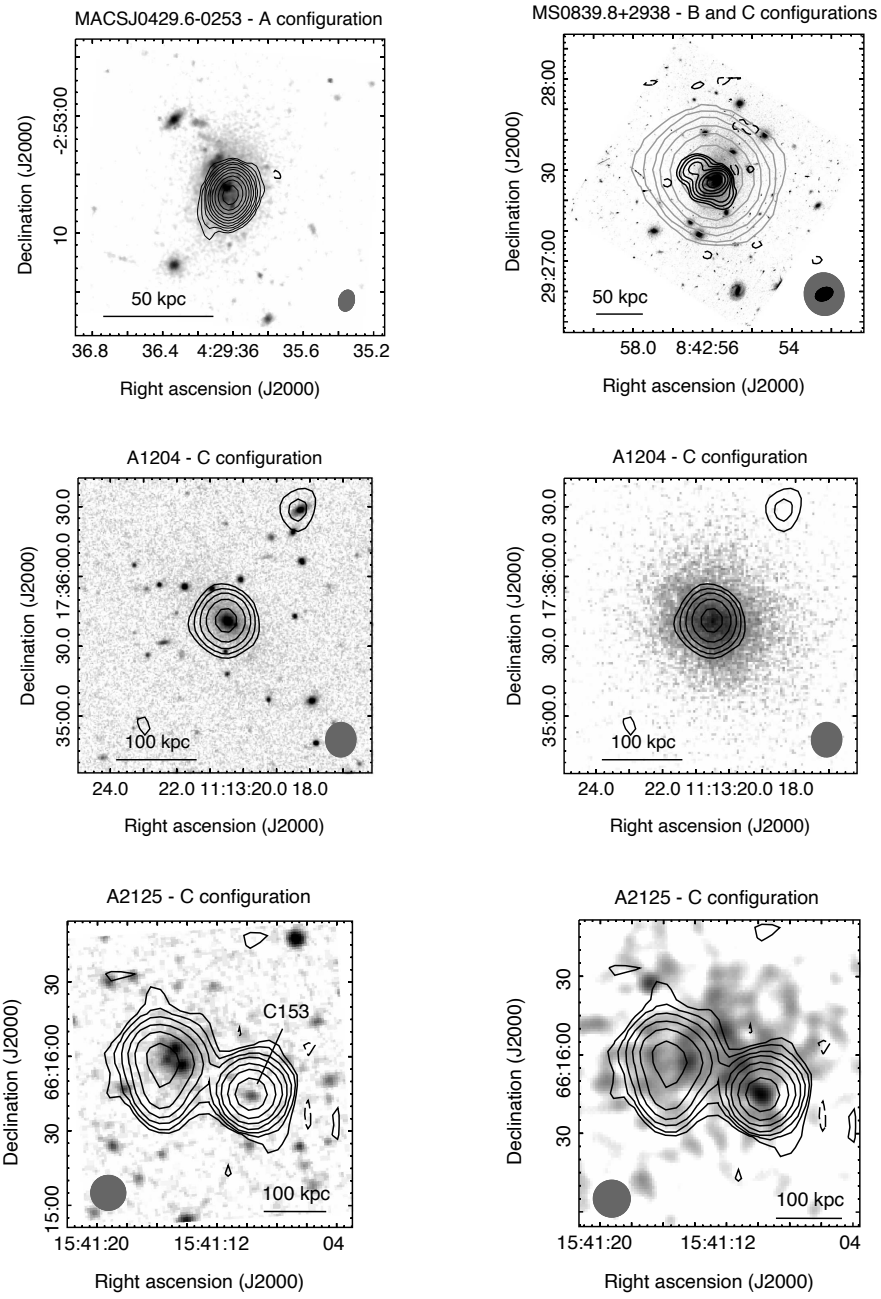

Figure 10. Upper panels: *VLA* 1.4 GHz radio images of MACS J0429.6-0253 (left) and MS 0839.8+2938 (right), overlaid on the preview HST WFPC2 images (programs 11103 and 11312). Middle panels: *VLA* 1.4 GHz radio image of A 1204, overlaid on the optical r-band SDSS image (left) and smoothed X-ray *Chandra* image in the 0.5-4 keV band (right). Bottom panels: *VLA* 1.4 GHz radio image of A 2125, overlaid on the optical POSS–2 red optical images (left) and smoothed X-ray *Chandra* images in the 0.5-4 keV band (right). In all panels, contours start at $+3\sigma$ and then scale by a factor of 2. When present, contours at -3σ are shown as dashed. Restoring beams (also shown as ellipses in the lower corner of each image) and *rms* noise values are as listed in Table 9.

Table 9. Properties of the *VLA* radio images

Cluster name	Configuration	FWHM, p.a. (″×″, °)	*rms* (μJy beam^{-1})	$S_{1.4\,\mathrm{GHz}}$ (mJy)	LDS (Mpc)
A 193	C	16 × 14, 15	40	60 ± 3	0.8[a]
	C+D	25 × 19, −4	35	61 ± 3	0.8
A 383	A	1.5 × 1.3, −10	40	41 ± 2	0.12
	C+D	23 × 18, 8	45	41 ± 2	2.8
MS 0440.5+0204	A	1.5 × 1.3, −48	30	43.6 ± 2.2[b]	0.12
	C	15 × 13, −13	65	43 ± 2	2.8[a]
MACS J0429.6-0253	A	1.8 × 1.3, −15	38	133 ± 7	0.2
	B	5 × 4, −2	40	138 ± 7	0.6
MS 0839.8+2938	B	6 × 4, −65	40	25 ± 1	0.4
	C	14 × 13, 12	53	26 ± 1	2.9[a]
A 1204	C	15 × 13, −3	28	1.8 ± 0.1	2.6[a]
A 2125	C	14 × 14, −3	58	19 ± 1	3.5[a]
A 2420	CnB	14 × 6, 0	50	198 ± 10	1.4[a]
	DnC	50 × 20, 0	65	197 ± 10	1.4
A 2556	CnB	14 × 8, 71	45	20 ± 1[c]	1.5[a]
	DnC	47 × 25, 77	60	22 ± 1	1.5
	CnB+DnC	17 × 12, 60	35	22 ± 1[c]	1.5

[a] Although the shortest baseline is the same as in D configuration, the surface brightness sensitivity to extended structure is significantly less that that of the D configuration, but still high enough to detect diffuse emission on the core scale at typical brightness of minihalos (Appendix B).

[b] Sum of the flux densities of the double source (33.0 ± 1.7 mJy) and head-tail radio galaxy (10.6 ± 0.5 mJy).

[c] Sum of the flux densities of the central radio galaxy (1.8 ± 0.1 mJy in the CnB image and 1.9 ± 0.1 mJy in the CnB+DnC image) and head-tail radio galaxy (18 ± 1 mJy and 20 ± 1 mJy).

Note—Column 1: cluster name. Column 2: *VLA* configuration. Columns 3: Full width half maximum (FWHM) and position angle (p.a.) of the radio beam. Column 4:image root mean square (*rms*) level (1σ) for $ROBUST = 0$ in IMAGR. Column 5: total flux density of the central radio emission. Column 6: largest linear structure detectable by the observation (LDS), as derived from the maximum angular scale that can be imaged reasonably well by *VLA* long-synthesis observations.

A 383. A single point source with 41 ± 2 mJy is detected at cluster central galaxy in all our images (Fig. 9, middle panels). Its size is < 5 kpc, based on a Gaussian fit on our highest resolution image, obtained from the combination of the A–configuration observations.

MS 0440.5+0204. A central extended radio source is detected in the C–configuration image (Fig. 9, bottom panels). At the higher-resolution of the A–configuration observation, the source separates into a ~ 30 kpc double, associated with the cluster central galaxy, and a head-tail radio galaxy, identified as a member galaxy ($z = 0.193$, Gioia et al. 1998). A total flux of 43.6 ± 2.2 mJy is measured on the C–configuration image. This value is consistent with the sum of the flux densities in the double (33.0 ± 1.7 mJy) and head tail (10.6 ± 0.5) measured at higher resolution.

MACS J0429.6-0253. An unresolved source is detected at the cluster center in both A– and B–configuration images (Fig. 10, left upper panel; see also Fig. 7), with a flux density of 133 ± 7 mJy and 138 ± 7 mJy, respectively. Based on the A–configuration image, the source is < 10 kpc in size.

MS 0839.8+2938. The C–configuration observation detects a central compact radio source, which the B–configuration reveals to be a 80 kpc-long, core-dominated double radio source (Fig. 10, right upper panel; see also Fig. 7). Its flux density is 26 ± 1 mJy (C configuration) and 25 ± 1 mJy (B configuration).

A 1204. An unresolved source (size < 40 kpc) is detected at the cluster center in the C-configuration image (Fig. 10, middle panels). Its flux density is 1.8 ± 0.1 mJy. An unresolved source is also detected by a slightly higher resolution

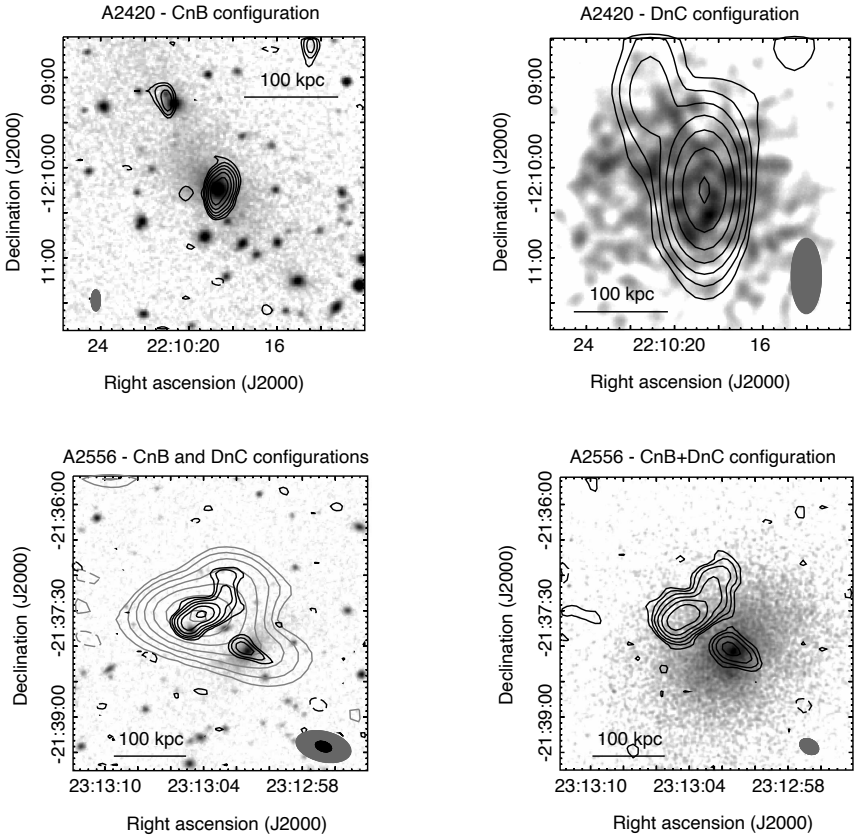

Figure 11. *VLA* 1.4 GHz radio images of A 2420 (upper panels) and A 2556 (bottom panels), overlaid on the optical POSS–2 red optical images (left) and smoothed X-ray *Chandra* images in the 0.5-4 keV band (right). In all panels, contours start at $+3\sigma$ and then scale by a factor of 2. When present, contours at -3σ are shown as dashed. Restoring beams (also shown as ellipses in the lower right corner of each image) and *rms* noise values are as listed in Table 9.

observation at 5 GHz with the *VLA* in C configuration (Hogan et al. 2015), with a similar flux of 1.8 mJy, implying a flat spectral index between 1.4 GHz and 5 GHz.

A 2125. A deep radio survey of the cluster region has been carried out by Owen et al. (2005) using the *VLA* at 1.4 GHz in its A and B configurations. An image of the central cluster region is presented in Owen et al. (2006). The region is occupied by a triple system of optical galaxies, each hosting an extended radio source, and a nearby bright compact radio galaxy, named C153. Here we present a lower resolution image of the cluster center, obtained from an archival *VLA* observation in C configuration (Fig. 10, bottom panels). The three central sources, individually detected by Owen et al., appear here blended into an single source with a total flux density of 19 ± 1 mJy. This value is in agreement with the the sum of the flux densities measured by Owen et al. (2005) for these three sources (19.3 mJy). C153 is unresolved in our image; its flux density of 22.9 ± 0.7 mJy is in good agreement with that reported by Owen et al. (22.9 mJy).

A 2420. A slightly extended radio source, oriented north-south and with a flux density of 198 ± 10 mJy, is detected at the position of the central galaxy in the CnB–configuration image (Fig. 11, left upper panel). In the DnC–configuration image (Fig. 11, right upper panel), the source has a flux of 197 ± 10 mJy. The compact radio galaxy visible to the north-east has a flux of 1.5 ± 0.1 mJy (CnB configuration) and 2.1 ± 0.1 mJy (DnC configuration).

A 2556. The CnB–configuration and combined CnB+DnC-configuration images (Fig. 11, bottom panels), show an extended radio source associated with the dominant cluster galaxy, with a size of ~ 65 kpc along the NE-SW axis. A radio galaxy with head-tail morphology is located at a projected distance of about 90 kpc from the central galaxy. The flux densities of these sources, measured on the combined image are 1.9 ± 0.1 mJy and 20 ± 1 mJy, respectively.

The two radio galaxies are blended together in the lower-resolution image from the DnC configuration (Fig. 11, left bottom panel)) with a total flux density of 22 ± 1 mJy.

B. RADIO SIZE AND AVERAGE SURFACE BRIGHTNESS OF MINIHALOS AND HALOS

In Table 10 we summarize the properties — frequency, angular resolution, sensitivity and the radius of the largest detectable structure (based on full-synthesis nominal values for *GMRT*, *VLA* and *WSRT*) — of the radio images used to estimate the extent of the radio sources in our statistical and supplementary samples (candidates are not included). For each source, the table also lists the measured radius (the average radius of a 3σ isocontour, § 2) and the ratio of the source average surface brightness to the *rms* noise level of the corresponding radio image.

Table 10. Properties of the radio images and central diffuse radio sources

Cluster name	ν (GHz)	FWHM ($''\times''$)	*rms* (1σ) (mJy/beam)	$\frac{LDS}{2}$ (Mpc)	$R_{\rm radio}$ (Mpc)	$\frac{<SB_{\rm radio}>}{1\sigma}$	Reference
Clusters with minihalos in statistical sample							
A 478	1.4	30×30	0.05	0.7	0.16	7.9	4
RBS 797	1.4	19×12	0.04	2.2	0.12	12.2	2
A 3444	0.6	7×7	0.04	2.0	0.12	10.4	3
A 1835	1.4	51×45	0.04	1.8	0.24	23.7	2
AS 780	0.6	6×4	0.07	1.9	0.05	17.0	5
RXC J1504.1−0248	0.3	11×10	0.10	3.3	0.14	22.7	6
A 2029	1.4	57×45	0.04	0.6	0.25	10.8	2
A 2204	1.4	6×5	0.03	0.16	0.05	7.1	4
RXC J1720.1+2638	0.6	8×6	0.03	1.4	0.14	28.1	7
A 2667	1.2	5×5	0.04	1.5	0.06	5.0	2
Clusters with minihalos in supplementary sample							
MACS J0159.8−0849	1.4	5×5	0.015	0.3	0.09	3.6	4
Perseus	0.3	51×77	1.4	0.9	0.13	98.7	8
MACS J0329.6−0214	1.3	5×5	0.03	1.2	0.07	6.3	2
2A 0335+096	1.4	30×27	0.04	0.3	0.07	10.2	2
A 907	0.6	5×5	0.05	1.5	0.06	11.0	2
ZwCl 3146	0.6	9×7	0.09	2.2	0.08	6.1	5
RX J1347.5−1145	1.4	17×17	0.04	2.6	0.26	30.4	2
MS 1455.0+2232	0.6	6×5	0.07	2.0	0.12	4.1	9
RX J1532.9+3021	1.4	3×3	0.01	0.3	0.10	4.3	4
Ophiuchus	1.4	110×60	0.12	0.25	0.25	5.8	2
RXC J2129.6+0005	0.6	11×11	0.11	1.9	0.08	4.8	5
Phoenix	0.6	14×6	0.04	3.4	0.23	6.7	10
Clusters with radio halos in statistical sample							
A 2744	1.4	50×50	0.09	2.0	0.8	12.7	34
A 209	1.4	60×40	0.05	1.5	0.5	9.3	12
A 401	1.4	60×60	0.08	0.6	0.4	3.8	2
PSZ1 G171.96−40.64	1.4	50×50	0.12	1.9	0.6	4.5	13
A 521	0.2	35×35	0.22	5.1	0.7	6.5	14
A 520	1.4	26×26	0.03	1.5	0.5	4.2	15
A 665	1.4	52×42	0.07	1.4	0.7	7.0	16
A 697	0.3	47×41	0.15	4.1	0.6	9.6	17
A 754	0.3	109×74	1.0	1.0	0.6	5.1	18
A 773	1.4	30×30	0.03	1.6	0.5	4.7	34

Table 10 continued

Table 10 *(continued)*

Cluster name	ν (GHz)	FWHM ($''\times''$)	rms (1σ) (mJy/beam)	$\frac{LDS}{2}$ (Mpc)	$R_{\rm radio}$ (Mpc)	$\frac{<SB_{\rm radio}>}{1\sigma}$	Reference
A 1300	0.3	28×28	0.50	4.3	0.5	4.2	11
A 1351	1.4	20×18	0.05	2.1	0.5	3.2	19
A 1443	0.3	27×27	0.36	3.9	0.6	1.8	20
A 1689	1.4	67×52	0.10	1.3	0.7	5.0	2
A 1758a	0.3	35×35	0.40	4.1	0.8	3.3	11
A 1914	1.4	50×45	0.05	1.3	0.6	16.7	21
RXC J1514.9−1523	0.3	53×41	0.27	3.4	0.7	5.5	22
A 2142	1.4	60×60	0.18	0.7	0.4	2.0	23
A 2163	1.4	45×60	0.05	1.5	1.0	23.4	24
A 2218	0.6	25×25	0.07	1.5	0.4	1.7	2
A 2219	1.4	50×45	0.07	1.6	0.7	18.1	21
A 2256	0.3	67×67	0.60	3.5	0.5	7.2	25
A 2261	1.4	50×50	0.05	1.6	0.5	2.8	26
CL 1821+643	0.3	30×26	0.20	4.5	0.4	8.6	27
RXC J2003.5−2323	1.4	35×35	0.03	2.1	0.9	9.4	28
A 2390	1.4	30×30	0.04	1.7	0.4	8.1	26
RXC J1314.4−2515	0.6	25×22	0.06	1.9	0.3	3.7	12
Clusters with radio halos in supplementary sample							
A 399	1.4	45×45	0.04	0.6	0.3	4.2	33
MACS J0417.5−1154	0.6	20×20	0.15	2.9	0.5	4.7	29
A 1995	1.4	30×30	0.05	2.1	0.3	4.4	30
A 2034	1.4	44×40	0.04	0.9	0.3	7.0	30
A 2255	0.3	54×64	0.10	3.7	0.8	15.7	31
A 2319	1.4	119×110	0.40	0.9[a]	0.6	6.4	32

[a] combination of two VLA pointings offset by $12.2'$.

NOTE—Column 1: cluster name. Columns 2–4: frequency, beam FWHM and rms noise (1σ, per beam) of the images used to measure the source radius. Images at 1.4 GHz are from *VLA* observations, all other frequencies are *GMRT* observations; for Perseus and A 2255 we used *WSRT* images. Column 5: radius of the largest linear structure detectable by the observations, as derived from the maximum angular scale that can be imaged reasonably well by long-synthesis observations with the *VLA*, *GMRT* and *WSRT*. Column 6: radius of the central diffuse radio source, defined as in §2, derived from the 3σ surface brightness isocontour. Column 7: ratio of the source average surface brightness ($SB_{\rm radio}$) and 1σ noise level of the image. Column 8: reference for the radio images. Reference code: (1) this work, (2) G17a, (3) G17b, (4) Giacintucci et al. (2014a), (5) Kale et al. (2015), (6) Giacintucci et al. (2011a), (7) Giacintucci et al. (2014b), (8) Sijbring (1993), (9) Venturi et al. (2008), (10) van Weeren et al. (2014), (11) Venturi et al. (2013), (12) Venturi et al. (2007), (13) Giacintucci et al. (2013), (14) Brunetti et al. (2008), (15) Vacca et al. (2014), (16) Giovannini & Feretti (2000), (17) Macario et al. (2010), (18) Macario et al. (2011), (19) Giacintucci et al. (2009a), (20) Bonafede et al. (2015), (21) Bacchi et al. (2003), (22) Giacintucci et al. (2011b), (23) Venturi et al. (2017), (24) Feretti et al. (2001), (25) Brentjens (2008), (26) Sommer et al. (2017), (27) Bonafede et al. (2014), (28) Giacintucci et al. (2009b), (29) Parekh et al. (2017), (30) Giovannini et al. (2009), (31) Pizzo & de Bruyn (2009), (32) Storm et al. (2015), (33) Murgia et al. (2010), (34) Govoni et al. (2001), (35) Vacca et al. (2015).

In Fig 12, we compare the measured source radii to the interval of linear scales that can be detected in the respective radio images. The minimum scale is set by the angular resolution of the image (average FWHM, Table 10). We note here that almost all clusters have complementary observations at higher resolution. The maximum scale is the radius of the largest structure that can be detected in this particular observation (Table 10). Even though the actual scale that can be reliably imaged by the observation can be less than the nominal value (due, for instance, to a short exposure or the exclusion of bad data at short baselines), the minihalo and halo radii are typically much less than $LDS/2$ (one exception is Ophiuchus). This indicates that the observations are not limited by the interferometric coverage; if there was emission outside the minihalo, provided sufficiently low noise, we should be able to detect it well beyond the cool core and, in most cases, on scales comparable to those of large halos. The other obvious instrumental limitation is the noise level — if minihalos and large halos were similar sources with a smoothly declining radial brightness profile, a more sensitive observation would yield a larger

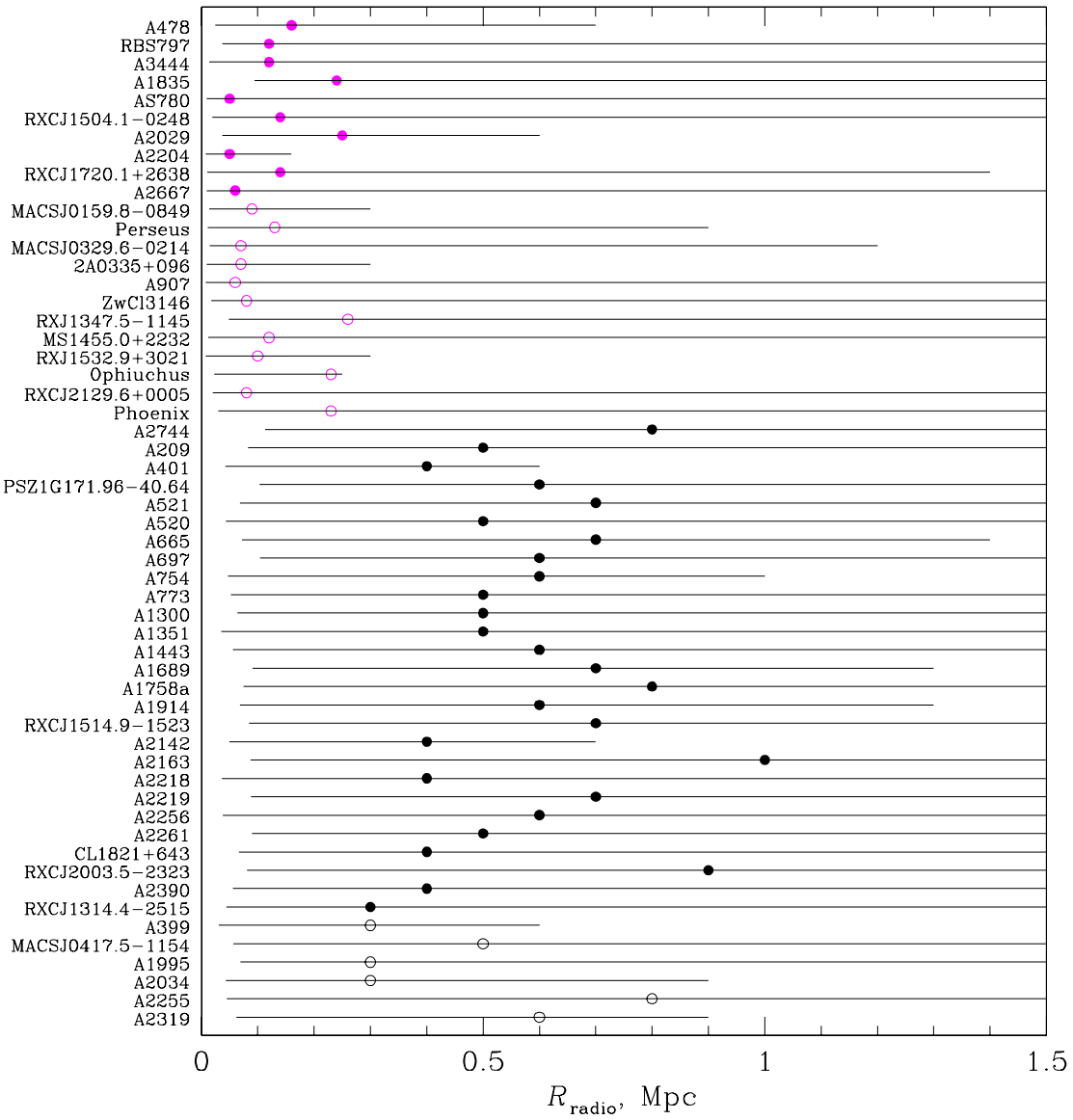

Figure 12. Radius of minihalos (magenta) and halos (black) in the statistical sample (filled symbols) and supplementary sample (empty symbols). Horizontal lines show the range of linear scales that can be detected in the corresponding radio images: the minimum scale is the angular resolution of the image, the maximum scale is the radius of the largest structure that can be imaged by the observations (Table 10).

radius of the 3σ isophote. In Fig. 13, we show the ratio of the source average surface brightness to the image *rms* noise (Table 10) as a function of the radius in kpc (left panel) or in beam sizes (right panel). There is no correlation between the signal-to-noise ratio and the radius of the halo; the signal-to-noise ratios for the minihalos are similar to those for the large halos and in several cases even slightly higher. This is in agreement with a similar plot for giant halos in Cassano et al. (2007). Based on Figs. 12 and 13, we conclude that most of the minihalo datasets used in this work possess the requisite sensitivity to detect diffuse emission on angular scales greater than the minihalo at a surface brightness level typical of large halos, thus the measured difference between the sizes of minihalos and large halos is physically meaningful. This answers a frequently asked question of whether minihalos are simply the peaks of larger halos in a cluster with the central density peak (and where the radio

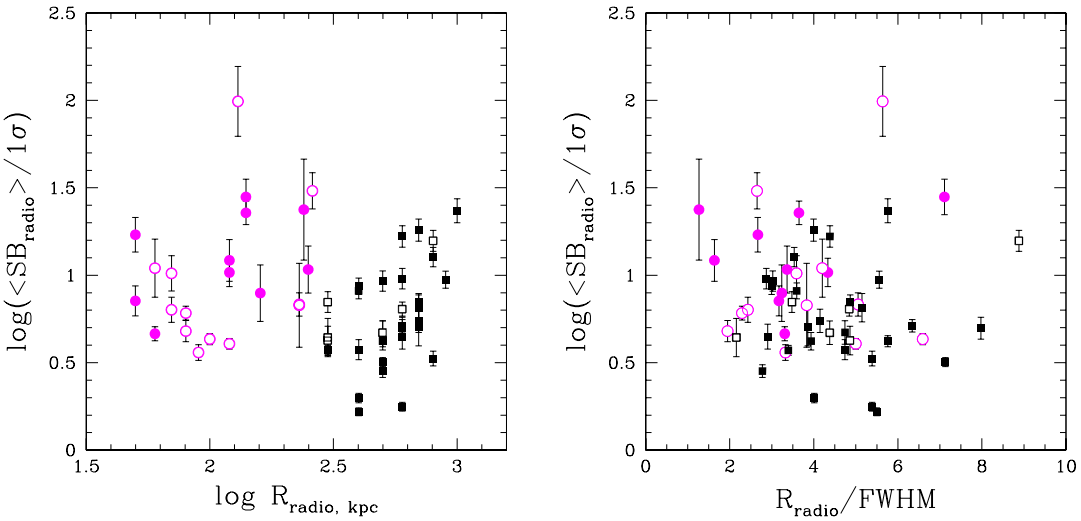

Figure 13. Ratios of the average surface brightness of minihalos (magenta) and large halos (black) to the *rms* noise level (per beam) of the corresponding radio images (Table 10). The ratios are plotted as a function of the radius in kpc (left) and beam sizes (right). Filled symbols are clusters in the statistical sample and empty symbols are those in the supplementary sample.

emission roughly follows the ICM density) — in such a picture, we would be able to detect the rest of the halo emission outside the cool core, and we do not.